



**HAL**  
open science

# Derivation of dielectric function and inelastic mean free path from photoelectron energy-loss spectra of amorphous carbon surfaces

Denis David, Christian Godet

► **To cite this version:**

Denis David, Christian Godet. Derivation of dielectric function and inelastic mean free path from photoelectron energy-loss spectra of amorphous carbon surfaces. *Applied Surface Science*, 2016, 387, pp.1125–1139. 10.1016/j.apsusc.2016.06.044 . hal-01372807

**HAL Id: hal-01372807**

**<https://univ-rennes.hal.science/hal-01372807>**

Submitted on 10 Oct 2016

**HAL** is a multi-disciplinary open access archive for the deposit and dissemination of scientific research documents, whether they are published or not. The documents may come from teaching and research institutions in France or abroad, or from public or private research centers.

L'archive ouverte pluridisciplinaire **HAL**, est destinée au dépôt et à la diffusion de documents scientifiques de niveau recherche, publiés ou non, émanant des établissements d'enseignement et de recherche français ou étrangers, des laboratoires publics ou privés.

APPLIED SURFACE SCIENCE

DOI: 10.1016/j.apsusc.2016.06.044

**Derivation of dielectric function and inelastic mean free path  
from photoelectron energy-loss spectra of amorphous carbon surfaces**

Denis David<sup>1</sup>, Christian Godet<sup>2</sup>,

<sup>1</sup> *Instituto de Física, Universidade Federal da Bahia, Campus Universitário de Ondina, 40.210-340 Salvador, Bahia (Brazil)*

<sup>2</sup> *Institut de Physique de Rennes (CNRS UMR 6251), Université Rennes 1, Campus Beaulieu - Bât. 11E - 35042 Rennes (France)*

*e-mail* : [christian.godet@univ-rennes1.fr](mailto:christian.godet@univ-rennes1.fr) / [denis.david@uol.com.br](mailto:denis.david@uol.com.br)

**Keywords:** XPS, energy loss, plasmon excitation, dielectric function, inelastic mean free path, amorphous carbon

## ABSTRACT

Photoelectron Energy Loss Spectroscopy (PEELS) is a highly valuable non destructive tool in applied surface science because it gives access to both chemical composition and electronic properties of surfaces, including the near-surface dielectric function. An algorithm is proposed for real materials to make full use of experimental X-ray photoelectron spectra (XPS). To illustrate the capabilities and limitations of this algorithm, the near-surface dielectric function  $\epsilon(\hbar\omega)$  of a wide range of amorphous carbon (a-C) thin films is derived from energy losses measured in XPS, using a dielectric response theory which relates  $\epsilon(\hbar\omega)$  and the bulk plasmon (BP) loss distribution. Self-consistent separation of bulk vs surface plasmon excitations, deconvolution of multiple BP losses and evaluation of Bethe-Born sensitivity factors for bulk and surface loss distributions are crucial to obtain several material parameters: (1) energy loss function for BP excitation, (2) dielectric function of the near-surface material (3-5 nm depth sensitivity), (3) inelastic mean free path,  $\lambda_p(E_0)$ , for plasmon excitation, (4) surface excitation parameter, (5) effective number  $N_{\text{EFF}}$  of valence electrons participating in the plasma oscillation. This photoelectron energy loss spectra analysis has been applied to a-C and a-C:H films grown by physical and chemical methods with a wide range of ( $sp^3$  /  $sp^2+sp^3$ ) hybridization, optical gap and average plasmon energy values. Different methods are assessed to accurately remove the photoemission peak tail at low loss energy (0-10 eV) due to many-body interactions during the photo-ionization process. The  $\sigma+\pi$  plasmon excitation represents the main energy-loss channel in a-C; as the C atom density decreases,  $\lambda_p(970 \text{ eV})$  increases from 1.22 nm to 1.6 nm, assuming a cutoff plasmon wavenumber given by a free electron model. The  $\pi-\pi^*$  and  $\sigma-\sigma^*$  transitions observed in the retrieved dielectric function are discussed as a function of the C hybridization and compared with literature results.

## 1. INTRODUCTION

Photoelectron Energy Loss Spectroscopy (PEELS) is a highly valuable non destructive tool derived from X-ray photoelectron spectroscopy (XPS) in applied surface science because it gives access to both chemical composition and electronic properties of surfaces, including the near-surface dielectric function. Although the outermost atomic layers often determine important characteristics of a solid, a clear understanding of the relationship between chemical, physical and electronic properties is still lacking for most non-crystalline surfaces. In particular, the dielectric function of the near-surface region contains crucial information to control a number of physical characteristics of thin film materials (plasmon energy [1-5], optical reflectivity [6], dispersive component of the surface energy [7, 8], secondary electron emission [9]) and for applications (plasmonics, antireflective or low emissivity coatings, adhesion and antifouling surfaces, scanning electron microscopy ...).

An accurate algorithm is required to make full use of experimental XPS-PEELS data. The near-surface dielectric function  $\epsilon(\hbar\omega)$  is derived from energy losses measured in XPS, using a dielectric response theory which relates  $\epsilon(\hbar\omega)$  and the bulk plasmon (BP) loss distribution. This algorithm being of general interest for researchers interested in solid surfaces with practical use, we have chosen to illustrate its capabilities and limitations using XPS-PEELS data obtained with a wide range of amorphous carbon (a-C) thin films. Let us recall that amorphous and diamond-like carbons represent prototypal materials in a variety of applications, including mechanics and tribology, electronics, electrochemistry, optics ...

In XPS-PEELS, the depth sensitivity is related to the inelastic mean free path of photoelectrons. Solid-state electron transport phenomena include a variety of processes with very different angular distributions of elastically and inelastically scattered electrons, respectively concentrated in an aperture of about  $\theta_T = 2T / E_0$  ( $T$  being the kinetic energy loss and  $E_0$  the kinetic energy of primary electrons) and spread out into an angle  $\theta = 1 / k_0 r$ , which is about  $10^2$  larger than  $\theta_T$  ( $k_0$  wave-vector of the incoming electron,  $r$  radius of the scattering atom) [3-5, 10, 11]. Elastic deflections arise from the interaction of the photoelectron with the (screened) Coulomb field of the nucleus; they contribute to increase the path length before electron escape at the surface boundary. Inelastic deflections, mainly at small angles, involve weakly bound electrons, i.e. in the valence band or the conduction band. The origin of the electron energy loss is that the induced electric field in the medium acts on the electron as it moves. [1-5, 12-13]. Plasma oscillations (or plasmons) are collective excitations which run as longitudinal charge density fluctuations through the volume of the solid (volume plasmon) and along its surface (surface plasmon). Their energy,  $T = \hbar\omega_p$ , is related to the oscillation

frequency  $\omega_p$  which depends on the density of loosely bound electrons, i.e. those for which  $\hbar\omega_p$  is large compared with their binding energy. Combinations of occupied valence band states with different hybridization may occur, e.g. in graphitic carbons, both  $\pi$  and  $\sigma+\pi$  plasmons (collective oscillation of all  $\sigma$  and  $\pi$  electrons) can be observed [14-17]. Because of the collective nature of plasmon losses, the low-loss spectrum is best described in terms of the complex dielectric function,  $\varepsilon(\hbar\omega)$ , of the medium [1-5].

This algorithm described in **Section 2** is based on physical grounds but corresponding appendices can be readily skipped by readers who wish to focus on practical results. The physics of XPS-PEELS is rather similar to REELS (Reflection Electron Energy Loss Spectroscopy), except for the presence of the electron-hole interaction and the lack of collimated beam in XPS where photoelectrons are generated homogeneously in the film over several microns. Hence, different loss energy dependent sensitivity factors must be considered in EELS, REELS and PEELS before retrieval of the dielectric function  $\varepsilon(\hbar\omega)$  (**Appendix 3**). In this work, an effective dielectric function is obtained by considering a weighted average of  $\varepsilon(\hbar\omega, q)$  over all allowed  $q$  wave vectors transferred by the photoelectron.

Well established methodologies have been reported in the literature to get the dielectric function from both Transmission Electron Energy Loss Spectroscopy (TEELS) [3, 4, 11] and REELS (Reflection Electron Energy Loss Spectroscopy). [10, 18-22] As compared to REELS and TEELS, the presence of the core hole in photoemission experiments is a difficulty which is addressed in this analysis of energy losses in order to retrieve  $\varepsilon(\hbar\omega)$ . Two phenomena occur during the photoionization transition: (i) collective excitation of valence electrons, i.e. generation of intrinsic plasmons and (ii) single particle excitations from occupied to empty states near the Fermi level, producing some tailing of the photoemission peak towards low kinetic energy. However, XPS provides unique capability to investigate hybridization and chemical composition, depth inhomogeneity, adventitious surface oxide or carbon contamination, which may be essential advantages in the interpretation of energy loss data.

In XPS-PEELS, elastic collisions may be neglected (in first approximation) on the basis of elastic and inelastic cross sections for C1s photoelectrons (970 eV) as discussed in **Section 5.2**. In contrast, in REELS, all detected electrons have undergone an elastic reflection in the back direction; besides the inclusion of elastic collisions in REELS modelling, this low-efficiency mechanism requires additional experimental considerations (signal-to-noise ratio, sample stability under irradiation, ...).

Self-consistent energy distributions of surface and bulk plasmon excitations are obtained from a dielectric model and their interplay is neglected on the basis of experimental emission angle

dependence, as  $B(E) + S(E) / \cos \alpha$  (**Section 4.3** and **Ref. 17**). However, spectral interdependence is expected as shown in **Figure C.1**.

In XPS-PEELS analysis, a major difficulty for the dielectric function retrieval is that two collective excitation mechanisms coexist and interfere, namely *intrinsic* plasmon losses which occur in the excitation process as a consequence of screening of the core hole by valence band electrons, and *extrinsic* plasmon losses which occur during photoelectron transport as a consequence of Coulomb interaction of valence electrons with the escaping photoelectron [5, 13]. In both cases, the screened Coulomb potential is related to the energy loss function (ELF)  $\text{Im}[-1/\epsilon(\hbar\omega)]$  and hence to the near-surface dielectric function,  $\epsilon(\hbar\omega)$ . The standard semi-classical analysis assumes that bulk, surface and intrinsic losses are uncorrelated processes; hence multiple plasmon losses can be separated using a partial intensity analysis [10, 19] or iteratively removed by successive convolutions. [20-22] We consider here that intrinsic loss will mainly affect the intensity of the first bulk plasmon rather than its energy distribution; in this sense, energy loss distributions of extrinsic and intrinsic plasmon are undistinguishable, for two reasons: (i) Bulk intrinsic plasmons of order 2 and higher usually have negligible intensity [5], (ii) quantum theory of plasmon excitation by low energy photoelectrons in Aluminum shows that the intrinsic contribution is nearly cancelled out by the interference term between intrinsic and extrinsic excitation [23]. Intrinsic surface excitations are also neglected.

In a three-step model of photoemission [5, 12, 24], different mechanisms contribute to XPS-PEELS spectra: (i) the core-level photoelectron peak (quasi-elastic peak) is asymmetrically broadened and shows a tailing over several eV (0-10 V range) towards lower kinetic energies as a consequence of the valence electrons response to the sudden photo-hole creation; single-electron scattering (exciting e.g. interband transitions) may also appear in this range; (ii) during photoelectron transport towards the surface, successive bulk plasmon excitations provide loss peaks at multiples of the ELF peak energy ( $E_P \approx 5-30$  eV), (iii) upon crossing the solid boundary, surface plasmon excitations are usually observed at lower kinetic energies and larger emission angles (with respect to the normal direction), but may be strongly attenuated for oxidized or rough surfaces. Careful treatment of raw XPS data is thus necessary to remove multiple excitations at high loss energy and the quasi-elastic peak at low loss energies, in order to retrieve the primary bulk loss spectrum,  $S_B(\hbar\omega)$ , of a subsurface region (5 nm depth sensitivity) over a typical energy range 0-50 eV.

To determine the ELF and the complex dielectric function of solid surfaces from X-ray photoelectron energy-loss spectra, this algorithm (**Section 2**) assumes a planar interface between a homogeneous solid and a vacuum. The loss function,  $\text{Im}[-1/\epsilon(\hbar\omega)]$ , is proportional to the "effective" energy loss

function for single bulk plasmon excitation divided by the sensitivity factor  $f(E)$ , due to the dependence of inelastic cross sections on energy and momentum conservation. This study addresses the critical removal of low-energy losses due to many-body interactions during the photo-ionization process. Several methods (subtraction of empirical analytic function, subtraction of a Doniach-Sunjić lineshape, [25] multiplication of raw spectra by a weighting function) are compared to obtain good signal-to-noise ratio while using most of the loss spectrum information in the 0-10 eV range.

A preliminary version of this inversion algorithm has been used to analyze PEELS data of a-Si:H films; the retrieved dielectric function was found to be consistent with the measured one in the UV-visible range. [26] Hydrogenated amorphous silicon was chosen as a reference material because electronic properties of device-grade a-Si:H are reproducible with a well-known dielectric function in the UV-visible range. In contrast, amorphous carbon (a-C) films can be prepared with a wide range of C atom densities,  $sp^2$  vs  $sp^3$  hybridization and nanostructuring of  $sp^2$ -C clusters since the growth mechanisms are highly sensitive to the deposition process [27]. This work compares PEELS characteristics of sputtered (SP), pulsed laser deposited (PLD) and plasma deposited (PL) a-C films with small surface roughness, corresponding to increasing  $sp^3/(sp^2+sp^3)$  hybridization ratio [28]. Further evaluation of the inversion algorithm is performed using a-C films either as-grown or after covalent grafting of densely-packed organic molecular monolayers (Section 3).

Finally, XPS-PEELS results for a-C films presented in Section 4 are further compared with previous data for a-Si:H [26]; due to the different valence electron densities and electronic bandgap in a-Si:H and a-C, different sensitivities of surface and bulk plasmon excitations can also be expected. To assess the hypotheses performed in this algorithm, the values of the inelastic mean free path (IMFP),  $\lambda_P(E_0)$ , for plasmon losses, the effective number,  $N_{\text{EFF}}$ , of valence electrons active in plasma oscillation and the surface excitation parameter (SEP) derived from this inversion algorithm are also discussed and compared with literature data (Section 5). The limits of the method and suggestions for further improvements will finally be addressed.

## 2. DIELECTRIC MODEL OF ENERGY LOSS SPECTROSCOPY

This Section recalls some basic physics of electron transport in solids useful for PEELS analysis, addressing bulk and surface plasmon excitations. This inversion algorithm is based on a self-consistent separation of surface and bulk plasmon loss distributions corresponding to a unique dielectric function, in contrast with previous inversion methods [29].

## 2.1. Bulk plasmon excitations

Owing to the collective nature of plasmon excitation, low-loss spectra are best described in terms of the complex dielectric function,  $\varepsilon(\hbar\omega)$ , of the solid (**Eq A.4** and **A.5**). For electrons travelling through an infinite medium, the differential inverse inelastic mean free path (DIIMFP) is the probability density per unit path length,  $K(E_0, \hbar\omega)$ , of losing an energy  $T = \hbar\omega$  [**1-5**]:

$$K(E_0, \hbar\omega) = (E_0 \pi a_0)^{-1} \int dq q^{-1} \text{Im}(-1 / \varepsilon(\hbar\omega)), \quad (1)$$

where  $E_0$  is the initial kinetic energy of the photoelectron,  $a_0$  is the Bohr radius, and  $q$  is the wave vector transferred from the electron (**Eq. (A.5)**).

$$q_{\pm} = (2m_0 / \hbar^2)^{1/2} [E_0^{1/2} \pm (E_0 - \hbar\omega)^{1/2}] \quad (2)$$

are  $q$  vector limits imposed by energy and momentum conservation during inelastic scattering. In addition, a cutoff wave vector transfer,  $q_c$ , and hence a cutoff scattering angle,  $\theta_c$ , are introduced to account for plasmon decay to single particle excitations (**Appendix B**). [**2, 5**] The depth resolution in XPS-PEELS is given by the inelastic mean free path (IMFP) for plasmon excitation,  $\lambda_P$ , defined by:

$$\lambda_P(E_0)^{-1} = \int d\hbar\omega K(E_0, \hbar\omega), \quad (3)$$

which is the average distance an electron travels between successive inelastic collisions, measured along its flight path.

## 2.2 Surface plasmon excitations and angular XPS-PEELS analysis

Collective excitations of valence electrons exist not only in the volume of a solid but also at its boundary, where longitudinal waves of charge density run along the surface as a polarisation wave. When a photoelectron crosses a planar boundary with an incidence angle  $\theta_i$ , the interface loss probability is given by **Eq A.14**, where the last term is equal to  $\text{Im}\left(\frac{1}{\varepsilon} - \frac{4}{1+\varepsilon}\right)$ ; the surface energy

loss function (SELF),  $S_S(\hbar\omega)$ , is thus peaked at  $\sqrt{2}E_p$ , where  $E_p$  is the peak energy of the bulk plasmon loss function,  $S_B(\hbar\omega)$ . The amplitude of the surface loss distribution is related to the surface excitation parameter (SEP) which is the average number of surface excitations an electron experiences when it crosses the surface once [**30-31, 32-33**]. The SEP being defined as the ratio between surface plasmon loss and photoemission peak intensities, SEP values are usually expressed through a modified Oswald equation:

$$P_s = \frac{1}{0.173 a E^{1/2} \cos \alpha + 1}, \quad (4)$$

(with  $E$  in eV), including a dimensionless material dependent parameter  $a$  which has been empirically correlated with plasmon energy  $E_p$  and optical gap  $E_G$  values [31, 32].

SEP values increase with increasing emission angle,  $\alpha$ . Angular photoemission spectra present twofold interest: a) assuming that  $S_S(\hbar\omega)$  follows the expected  $(b/\cos\alpha)$  dependence, decomposition of XPS-PEELS spectra into pure surface and pure bulk losses can be performed [17]; b) a quality criterion of the inversion algorithm can be defined by comparing the angular dependence of the retrieved  $S_S(\hbar\omega)$  with  $(b/\cos\alpha)$  behaviour. The latter approach is developed in Section 4.3 using surface modification of a-C (PLD) by covalent immobilization of an ester-terminated OML.

### 2.3. Inversion method to determine the dielectric function

After data selection in a range where a single core level (with zero-loss kinetic energy  $E_0$ ) contributes to energy losses, the inversion method used to determine the dielectric function from plasmon loss spectra is made of eight steps:

(1) Elimination of loss features due to X-ray source satellites (e.g. for non-monochromatic Mg X-rays,  $K\alpha_3/K\alpha_{1,2} = 0.08$  and  $K\alpha_4/K\alpha_{1,2} = 0.04$ ) [34] decreases the relative intensity of plasmon losses ; in the following, “monochromatized”  $J(T)$  spectra will be used after satellite removal.

(2) Separation of an asymmetric quasi-elastic peak at low kinetic energy using either a *subtraction* method (mirror operator for the symmetric part and fitting an empirical analytic function to the peak tail) or a *weighting* method where the total plasmon loss distribution  $S_P(T) = J(T) \sigma(T)$  is the product of the measured loss spectrum  $J(T)$  times a smooth sigmoid function  $\sigma(T)$ :

$$\sigma(T) = 0 \text{ for } T \leq E_G \text{ and } \sigma(T) = 1 - \exp\left(-\left(\frac{T - E_G}{\Delta E_{SIG}}\right)^2\right) \text{ for } T > E_G, \quad (5)$$

where  $T$  is the loss energy and  $E_G$  the gap of the material that can be determined by optical methods; this weighting method proposed previously (M4 in [26]) gives a good signal-to-noise ratio while using most of the loss spectrum information in the 0-10 eV range. Alternative weighting functions (e.g. polynomial or rational functions) have also been explored, leading to basically identical results.

(3) Extraction of single loss distribution  $S_B(T)$  from the multiple plasmon signal following Werner method [10] where the spectral shape is a superposition of the energy distributions for  $n$ -fold inelastically scattered electrons.

(4) Extrapolation of the single loss distribution  $S_B(T)$  to high loss energy (using a power-law function, typically above 50 eV for a-C) to allow a correct Kramers-Kronig integration.

(5) Derivation of  $S_B(T) / f_C(T)$  and application of the Kramers-Krönig transform (Eq C.3), using optical  $n(0)$  value in the low energy limit, to get the normalized ELF,  $Im(-1 / \epsilon(\hbar\omega))$ .

- (6) Application of the Kramers-Krönig transform to obtain  $Re(-1 / \epsilon(\hbar\omega))$  from  $Im(-1 / \epsilon(\hbar\omega))$ , and calculation of the real and imaginary parts of the dielectric function.
- (7) Removal of the first-order  $S_s(T)$  and its combination with multiple BP from PEELS data,  $J(T)$ , using the approximated complex dielectric function.
- (8) Derivation of the IMFP,  $\lambda_P(E_0)$ , for plasmon losses, the effective number,  $N_{EFF}$ , of valence electrons active in plasmon oscillation and the surface excitation parameter (SEP) using Bethe-Born factors  $f_C(T)$  and  $g(\alpha, T)$  for inelastic scattering (**Appendix A**).

Steps 3-7 are performed iteratively until convergence of both ELF shape and intensity is reached. Whereas steps 1 and 4 are trivial, other critical steps deserve some particular comments. The photoemission peak can be broadened over several eV toward the low kinetic energy side by: (i) many-body interactions related to the photo-hole screening by valence electrons during photoelectron production [35-36]; (ii) single electron inelastic scattering [3 Egerton]; (iii) inter band transitions [5, 2]. Effect (i) depends on the joint density of states near the Fermi level, hence it can be safely ignored in amorphous semiconductors but it should be considered in semimetal graphitic carbons [37]; however, a Doniach-Sunjić line shape has been fitted to  $J(E)$  near the zero loss peak maximum (typically from  $J_{MAX}$  to  $J_{MAX} / 2$ ) with reasonable singularity index values,  $\alpha_{DS}$ , in the range 0.04-0.15, but its subtraction provides non-physical results for a-C films as far as  $\epsilon(\hbar\omega)$  and  $N_{EFF}$  values are concerned. This issue will be considered in a separate work and justifies our more empirical approach.

Vibrational and recoil effects are negligible as compared with X-ray source width and analyzer resolution. However, the photoemission peak can also be asymmetrically broadened by the presence of various chemical environments, such as  $sp^2$  and  $sp^3$  hybridizations in a-C [28] or silicon suboxides  $SiO_x$  in  $Si2p$  spectra of a-Si:H surfaces.

In **step 5** of PEELS analysis, independent determination of the refractive index  $n(0)$  in the sub gap region is required to derive the dielectric function and the inelastic mean free path for plasmon energy losses ( $\lambda_P$ ). XPS spectra taken at different  $\alpha$  angles are useful to evaluate the SEP value and to check that the derived dielectric function,  $\epsilon(E)$ , is obtained self-consistently.

### 3. EXPERIMENTAL METHODS

This Section gives experimental details on a-C film deposition, covalent immobilization of densely packed monolayers of linear alkene molecules, spectroscopic ellipsometry (SE) and XPS-PEELS characterizations.

#### 3.1 Deposition processes

Hydrogenated amorphous carbon (a-C:H) films (~50 nm thick) with high  $sp^3$  content [28] were grown at 200°C on crystalline silicon Si(100) substrates using the radiofrequency plasma decomposition of ethylene in a turbo-pumped high vacuum chamber [38].

Pulsed Laser Deposition of amorphous carbon (a-C) films (30-60 nm-thick) was performed at room-temperature using a KrF laser (Tuilaser Excistar, 248 nm, 2 Hz, 20 ns pulse width) and a rotating glassy carbon target (Sigradur G, HTW) inserted in a turbo-pumped high vacuum chamber [39]. The pulse energy (150 mJ) corresponds to a fluence of  $7.5 \text{ J}\cdot\text{cm}^{-2}$ . After deposition, nitrogen was introduced in the chamber and the carbon film was quickly transferred to the XPS setup or to the grafting setup under a dry nitrogen atmosphere.

Magnetron sputtering (300 W) of a graphite target [40] has been performed either in pure Ar (1 Pa) (a-C) or in Ar+H<sub>2</sub> mixtures (1 Pa) (a-C:H) leading to amorphous carbon films grown at room temperature with high  $sp^2$  content [28].

#### 3.2 Thermal grafting of organic monolayers

A low-temperature (160°C) liquid-phase thermal process described previously [39] was used to react linear ethyl undecylenate  $\text{CH}_2=\text{CH}(\text{CH}_2)_8\text{-COOC}_2\text{H}_5$  molecules with a-C surfaces. After overnight exposure at 160°C, and cooling, the modified surfaces were rinsed copiously to eliminate physisorbed molecules.

#### 3.3 Spectroscopic ellipsometry

Spectroscopic ellipsometry (SE) experiments were performed in the range 0.7-4.7 eV, at an incidence angle of 70°, using a Horiba (UVISEL) ellipsometer, and analyzed with a multilayer model including a Tauc-Lorentz parameterization [41] suitable to describe the dielectric function of amorphous semiconductors (a-C, a-Si:H). This single-oscillator model gives the value of the refractive index extrapolated to 0 eV,  $n(0)$ , which is needed in the inversion algorithm, and the Tauc gap energy at the onset of optical absorption, which is useful in the definition of the sigmoid function (Table I).

### 3.4. X-ray photoelectron spectroscopy

XPS measurements were performed in an analysis chamber (base pressure in the  $10^{-10}$  mbar range) equipped with a VSW X-ray source (Mg  $K\alpha$ , 1253.6 eV) and Omicron HA100 hemispherical electron energy analyzer. By rotating the sample, angular analysis can be performed from  $\alpha = 0^\circ$  (normal) to  $75^\circ$  emission angles. The ( $sp^3 / sp^2+sp^3$ ) hybridization ratio (**Table I**) and binding energy difference (0.8 eV) measured using a monochromatic Al  $K\alpha$  X-ray source [28] are useful parameters to describe the shape of the C1s no-loss peak. For core-level loss spectroscopy, plasmon losses were measured with a 1.3 eV resolution (44 eV pass energy) with a typical count rate of  $8 \times 10^4$  counts  $eV^{-1}$  near the plasmon loss peak maximum at  $E_P$  (signal-to-noise ratio  $\approx 100$ , **Fig. 1**). The no-loss peak is thus slightly broadened, with an apparent full width FWHM  $\approx 2.1$  eV in the case of carbon surfaces.

**Table 1 :** Characteristics of a-C films derived from XPS and SE :  $sp^3 / (sp^3 + sp^2)$  hybridization ratio ( $\pm 0.05$ ), binding energy at the photoemission peak maximum ( $\pm 0.05$  eV), refractive index  $n(E \approx 0)$  ( $\pm 0.03$ ), Tauc gap energy at the onset of optical absorption ( $\pm 0.2$  eV), apparent plasmon excitation energy  $E_{P\text{ APP}}$  ( $\pm 0.3$  eV) at maximum in  $J(T)$  (**Fig. 1b**).

Material	$sp^3$ fraction	C 1s binding energy (eV)	Refractive index $n(0)$	Tauc gap (eV)	$E_{P\text{ APP}}$ (eV)
<b>a-Si:H (Plasma)</b>	<b>1.0</b>	---	<b>3.45</b>	<b>1.6</b>	<b>17.0</b>
<b>a-C:H (Plasma)</b>	<b>0.88</b>	<b>285.6</b>	<b>2.0</b>	<b>2.5</b>	<b>21.5</b>
<b>a-C (PLD)</b>	<b>0.52</b>	<b>285.6</b>	<b>2.50</b>	<b>0.6</b>	<b>30.5</b>
<b>a-C (Sputtering)</b>	<b>0.18</b>	<b>284.8</b>	<b>2.30</b>	<b>0.4</b>	<b>28.0</b>
<b>a-C:H (Sputtering)</b>	<b>0.13</b>	<b>285.2</b>	<b>1.90</b>	<b>0.5</b>	<b>25.5</b>

#### 4. EXPERIMENTAL RESULTS

This Section presents XPS-PEELS data obtained with the bare a-C surfaces described in **Table I** and with a-C (PLD) after immobilization of an ester-terminated OML. Angular measurements were used to check that surface plasmon excitation follows the expected  $(b/\cos\alpha)$  law and the dielectric functions are derived from PEELS data at normal emission ( $\alpha = 0^\circ$ ).

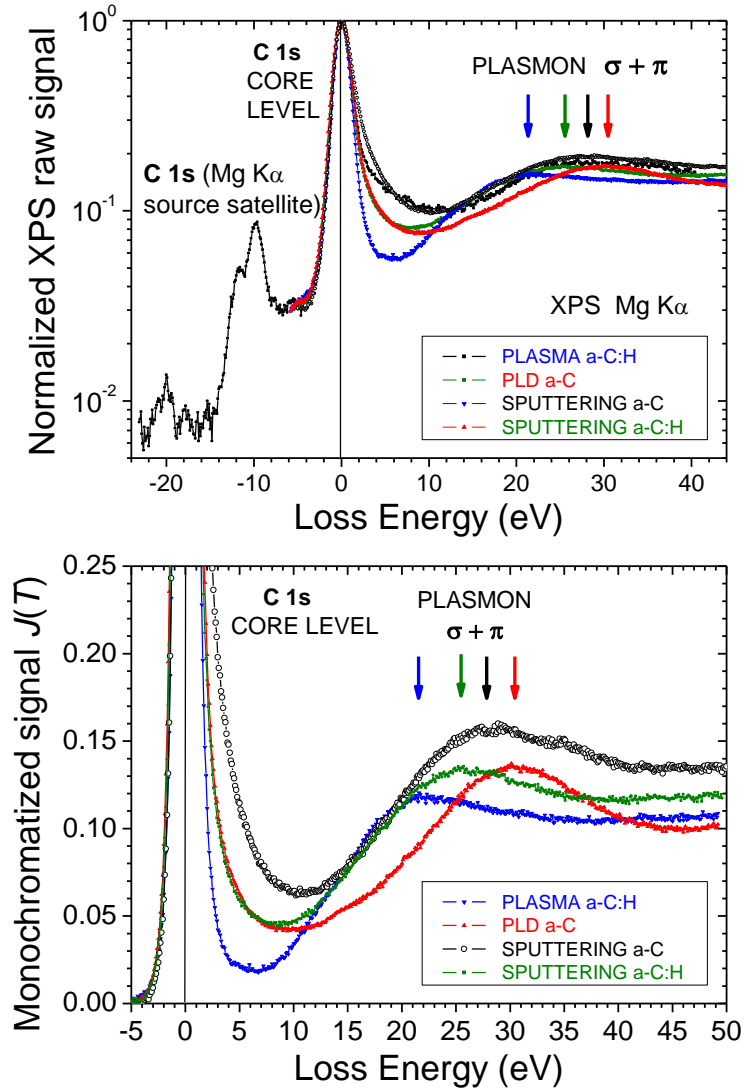


**Fig. 1.** XPS spectra (emission angle  $\alpha = 0^\circ$ ) for different a-C films with variable  $sp^2$ - $sp^3$  content and  $(\sigma + \pi)$  plasmon energy : a) Raw XPS spectrum obtained with non-monochromatic Mg  $K\alpha$  X-ray source; b) numerically monochromatized loss spectra  $J(T)$  using satellites  $K\alpha_3/K\alpha_{1,2} = 0.08$  and  $K\alpha_4/K\alpha_{1,2} = 0.04$  at -8.4 and -10.2 eV, respectively.

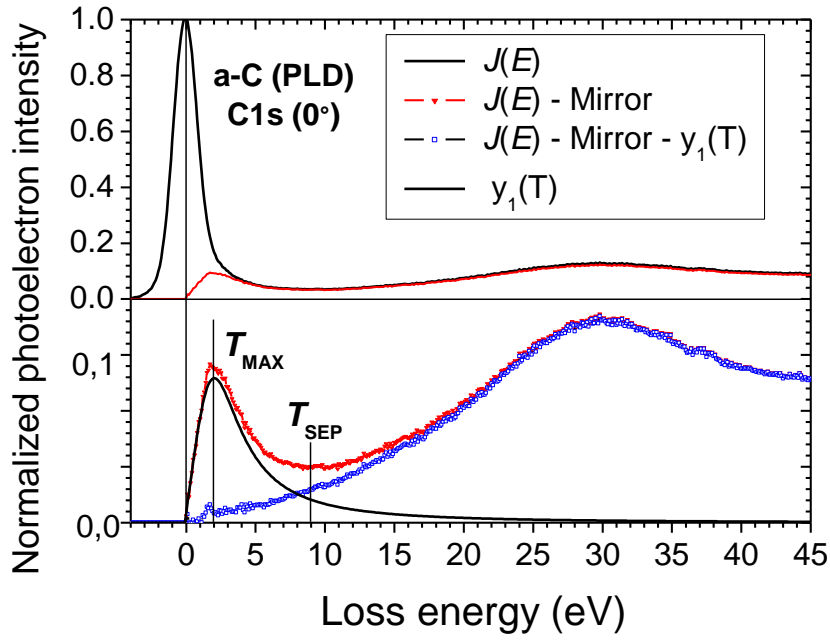


**Fig. 2.** Removal of the photoemission peak from the normalized  $J(T)$  spectrum of a-C (PLD) : the mirror subtraction method (see text) is followed by adjustment of an analytic  $y_1(T)$  function ( $m = 3$ ) to obtain the sum of all plasmon losses (open blue circles).

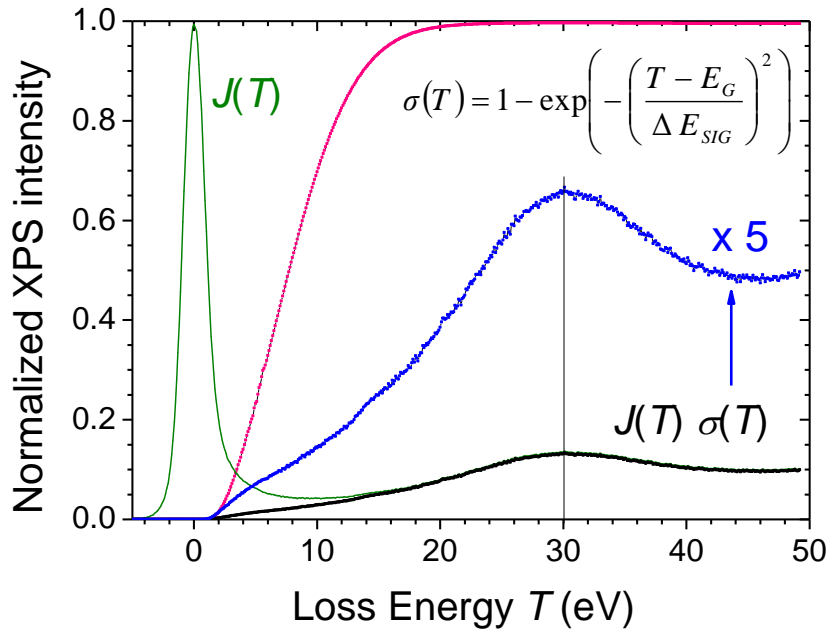


**Fig. 3.** Removal of the photoemission peak from the normalized  $J(T)$  spectrum of a-C (PLD) using a sigmoid weighting function (**Eq. 5**) with  $\Delta E_{SIG} = 8.5$  eV,  $E_G = 0.6$  eV.

#### 4.1 Suppression of the photoemission peak

Raw photoelectron energy-loss spectra of four a-C films are shown in **Figure 1a**, after setting the energy of the core level peak maximum to zero loss energy. In a-C films with variable  $sp^3 / (sp^2 + sp^3)$  ratio, this compensates for the different average binding energies of the C1s core level (**Table I**) due to different content of  $sp^2$  (284.8 eV) and  $sp^3$  (285.6 eV) hybridization components.

Using non-monochromatic source, the loss spectra corresponding to the C1s core level contain contributions from the different Mg  $K\alpha$  satellites, which were numerically removed in **Figure 1b**. The main energy loss peak attributed to the  $(\sigma + \pi)$  plasmon is very broad for all carbon surfaces; its apparent peak position in  $J(E)$  shows considerable increase from the plasma-deposited a-C:H ( $E_{P\text{ APP}} = 21.5$  eV) to the pulsed-laser deposited a-C ( $E_{P\text{ APP}} = 30.5$  eV). The  $(\sigma + \pi)$  plasmon is separated from the quasi-elastic peak by a minimum signal at energy  $T_{SEP}$  (typically 5-10 eV for a-C).

For the plasma-deposited a-C:H with small  $sp^2$  C content and wide band gap ( $E_T \approx 2.5$  eV), the core level peak is nearly symmetrical and decreases to a minimum value close to zero around a loss energy  $T_{SEP} = 6.5$  eV. In contrast, other carbon surfaces show a strong asymmetry with a wide tail extending up to 10 eV in the case of the  $sp^2$ -rich sputtered a-C. This feature has been attributed to the existence of  $\pi$ -plasmon excitations, expected near 5-7 eV [28]. In this hypothesis, the weaker tailing observed in hydrogenated sputtered a-C:H would indicate that the  $\pi$ -plasmon strength is not uniquely related to the  $sp^2$  C content, possibly because incorporation of carbon-hydrogen bonds may change the carbon film nanostructure. Alternatively, an asymmetric photoemission peak is expected due to many-body effects including transitions from filled to empty states near the Fermi level, as observed in organic compounds [37].

To eliminate the quasi elastic peak, a first approximation consists in removing a symmetric profile using the high kinetic energy data and a mirror operation. Removal of a symmetric peak leaves a strong signal at low loss energy (red curve  $y(T)$  in **Fig. 2**), peaked at  $T_{MAX} = 1-3$  eV for a-C surfaces, which clearly departs from the expected  $\pi$ -plasmon energy. Since the strong residual signal impedes accurate determination of the dielectric function, alternative methods have been considered using the fact that, at low loss energy  $T$ , the ELF grows linearly with  $T$  for a Lorentz dielectric function : a) in EELS spectra, Egerton [3] suggested to ignore the transition region up to  $T_{SEP}$  and to set a linear variation from 0 to  $T_{SEP}$ ; b) an analytic function  $y(T) = y_1(T) + y_2(T)$  can be adjusted to the data (as illustrated in **Fig. 2**) where the first term represents the photoemission peak tail function, e.g.  $y_1(T) = d T / (1 + cT^m)$ , and  $y_2(T) = aT$  represents the linear  $T$  dependence of the ELF. The former

method suppresses considerable information over a broad energy range (up to  $T_{SEP}$ ) while the latter subtraction leads to some unacceptable noise level for further PEELS analysis [26].

In this work, we consider the total loss distribution  $S_P(T)$  (surface plasmon and multiple bulk plasmon) as being the product  $S_P(T) = J(T)\sigma(T)$  of the measured loss spectrum  $J(T)$  times a monotonic weighting function  $\sigma(T)$  (Eq.5). The weighting function may be empirical or it may fulfil physical constraints, e.g. the ELF has linear energy dependence  $S_p(T) \approx aT$  at low loss energy. As shown in Fig. 3, using a smooth (sigmoid) weighting function provides a loss function very similar to the subtraction method while keeping a good signal-to-noise ratio below  $T_{SEP}$ .

#### 4.2. Separation of multiple order bulk plasmons

Figure 4 shows the separation of multiple bulk plasmon contributions for a-C (PLD) after a first iteration which neglects surface excitations ( $SEP = 0$ ). To illustrate the spectral analysis method and avoid any errors due to data extrapolation, the loss energy range was extended to 90 eV. Since multiple loss distributions are self-convolutions with the ELF, we define a series of spectral functions  $L_{n+1}(T) = \int L_n(T') \omega(T - T') dT'$  where  $L_1(T) = \omega(T) = \lambda_p(E_0) K(E_0, T)$  is the normalized differential inverse inelastic mean free path (DIIMFP). Following Werner method, separation of  $S_p(T) = C_n \sum_{n=1}^{\infty} L_n(T)$ , into multiple plasmon contributions requires determination of the partial intensity,  $C_n$ , values by performing iterative elimination of losses at order  $n$ , centered near ( $n E_p$ ).

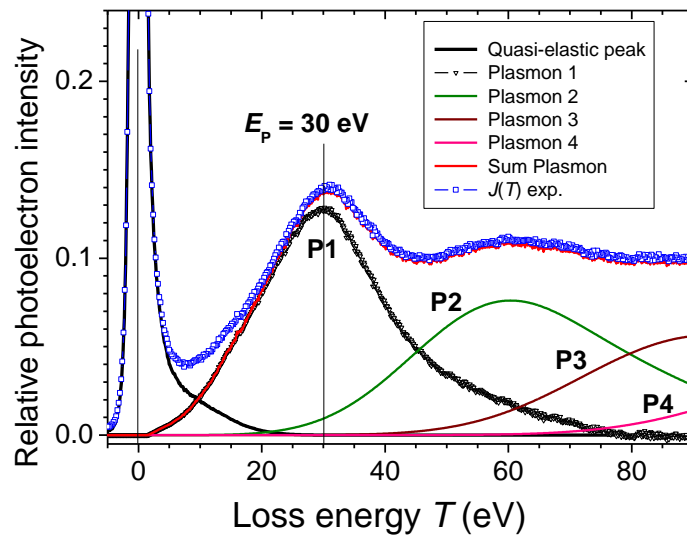


**Fig. 4.** Deconvolution of plasmon losses in PLD a-C ( $\alpha = 0^\circ$ ) up to 4<sup>th</sup> order after application of the sigmoid method ( $\Delta E_{SIG} = 10$  eV,  $E_G = 1.3$  eV). In this case, the ELF obtained after step 3 of the algorithm (neglecting surface plasmon,  $SEP = 0$ ) is very similar to the final ELF result in Fig. 7a.

In practice, additional constraints can be imposed, such as a smooth decrease of the ELF toward zero at high loss energy. The single loss function derived from PEELS analysis has a broad peak maximum near  $E_P \approx 30$  eV. Since the ELF extends up to 80 eV, i.e.  $T \approx 2.5 E_P$ , convolutions up to third-order at least are required to derive the single loss function (**Fig. 4**) and the effective number of electrons participating in plasma oscillations (**Eq. C7-C8**) will eventually converge beyond this energy loss value.

### 4.3. Angular PEELS analysis (OML-grafted a-C surface)

The accuracy of surface plasmon removal is illustrated using a broad range of XPS emission angles ( $0^\circ$  to  $75^\circ$ ) for an ester-terminated OML grafted to a PLD a-C film. At larger emission angles, the  $\text{COOH}$  functionality is observed as a shoulder shifted by 3.5 eV from the main C1s peak (**Figure 5**). In this case, higher order bulk plasmon losses were removed using the universal background function proposed by Tougaard [42] as described in a previous report [17]. XPS-PEELS spectra show a bulk plasmon loss peak centered near 28.5 eV, along with strong surface plasmon located near 19.5 eV.

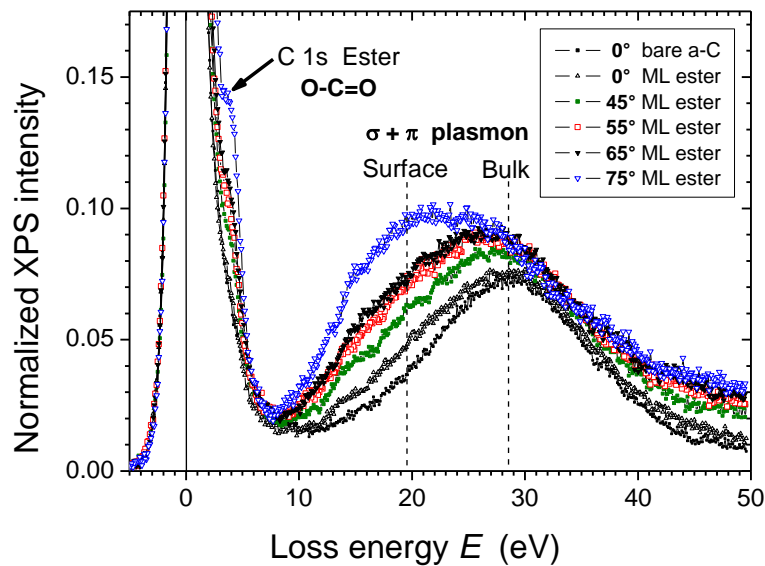


**Fig. 5.** Angular dependence of the C1s core level photoelectron loss spectrum of PLD a-C grafted with an ester-functionalized molecular monolayer. In this plot, the universal Tougaard function for background subtraction has been used [17].

The photoemission peak was subsequently eliminated using the sigmoid method and the ELF,  $\text{Im}[-1/\epsilon(E)]$ , was calculated either without (**Fig. 6a**) or with (**Fig. 6b**) surface plasmon subtraction. The computation of the surface plasmon distribution and iterative adjustment of its strength provides a

nearly perfect coincidence of all  $\text{Im}[-1/\epsilon(E)]$  curves, over a broad emission angle range. The a-C surface grafted with a dense molecular monolayer is characterized by a very intense surface plasmon (in contrast with bare a-C) with energy distribution given by **Eq. (C.6)** and relative amplitude accurately fitted by a  $(b/\cos\alpha)$  law.

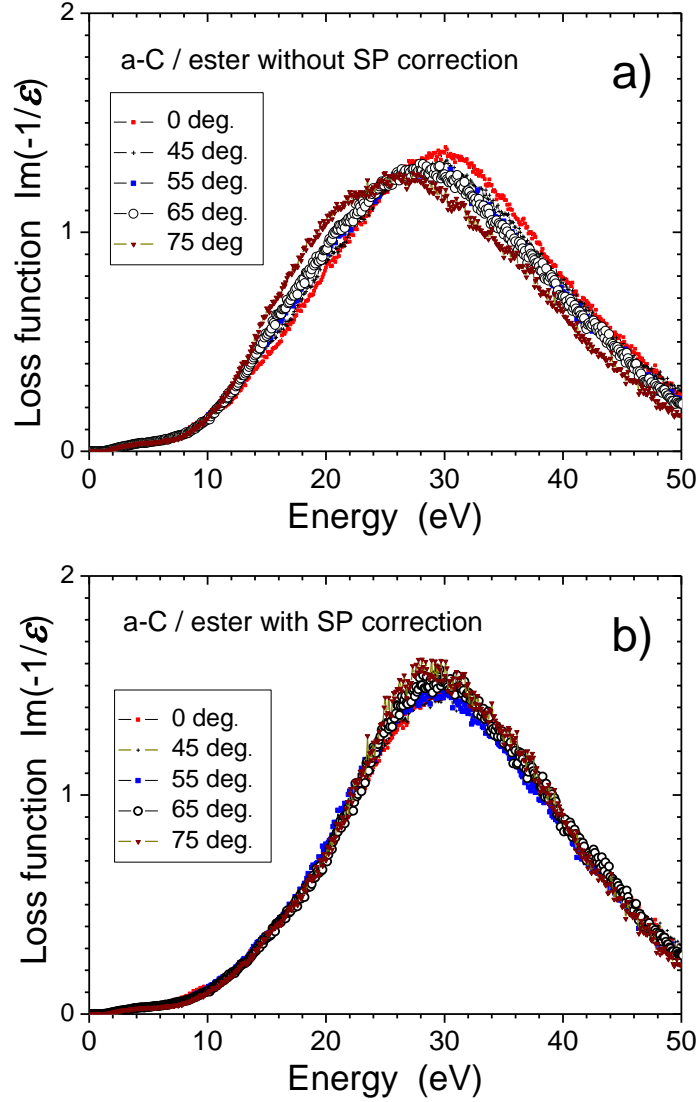


**Fig. 6.** First order plasmon loss distribution,  $\text{Im}[-1/\epsilon(E)]$  of ester-grafted a-C calculated for XPS data at various emission angles (**Fig. 5**), without (a) and with (b) computing surface plasmon losses ( $n(E \approx 0) = 2.50$ ,  $E_G = 1.0$  eV,  $\Delta E_{\text{SIG}} = 11.0$  eV).

#### 4.4. Dielectric function of a-C surfaces with variable hybridization

The last step of the algorithm is the retrieval of the complex dielectric function, after normalizing the ELF,  $\text{Im}[-1/\epsilon(E)]$ , using the bulk index  $n(E \approx 0)$  obtained by SE. The SELF is then calculated using the approximated complex dielectric function, its intensity is adjusted and removed from XPS-PEELS data,  $J(E)$ , to calculate again the ELF and the dielectric function, until convergence is obtained. Since the SELF is negative near  $E_P$  (**Fig. C.1**), this adjustment enhances the relative intensity and increases the peak energy of the bulk plasmon energy distribution.

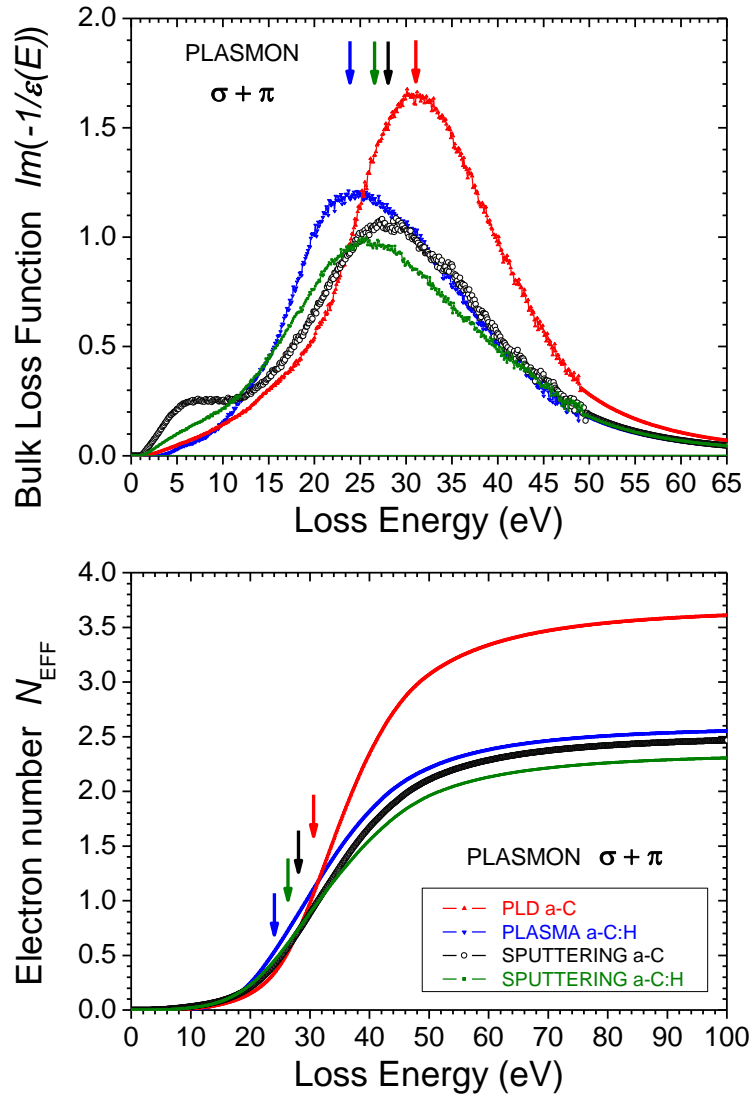


**Fig. 7.** a) Energy loss function; b) effective number,  $N_{\text{EFF}}$ , of valence electrons active in plasmon oscillation (**Eq. (C.8)**) assuming C atom density of  $1.6 \times 10^{23} \text{ cm}^{-3}$  (as found in diamond). The ELF is extrapolated towards high loss energy as  $E^{-6}$ .

As expected from their variable  $sp^2$ - $sp^3$  hybridization, very different bulk ELF are obtained for the four amorphous carbon films, both in the  $\sigma+\pi$  plasmon region and in the low energy range (**Fig. 7a**). Due to the shape of the SELF distribution, the bulk ELF peak energy is slightly higher than the apparent value observed in raw  $J(E)$  spectra (**Fig. 1b, Table I**); it decreases in the series PLD a-C (31 eV) > SP a-C (28 eV) > SP a-C:H (26.5 eV) > PL a-C:H (24 eV). The bulk ELF intensity below 10 eV increases with increasing  $sp^2$  content: PL a-C:H < PLD a-C < SP a-C:H < SP a-C. However, quantification of the  $sp^2$ - $sp^3$  hybridization from PEELS data is beyond the scope of this work.

The  $N_{\text{EFF}}(E)$  values given in **Fig. 7** (obtained using a hypothetical atom density of  $1.6 \times 10^{23} \text{ cm}^{-3}$ , as in diamond) saturate beyond 80 eV. Variation in the  $N_{\text{EFF}}$  plateau value indicates that the atom density of amorphous carbon decreases in the series a-C (PLD) > a-C:H (PL) > a-C (SP) > a-C:H (SP). This result follows from the variation of the bulk ELF peak intensity. The IMFP for plasmon losses,  $\lambda_P$  (970 eV), obtained from XPS-PEELS analysis is found to increase from 1.22 nm to 1.60 nm as the  $N_{\text{EFF}}$  value, i.e. the atom density, decreases (**Table II**).

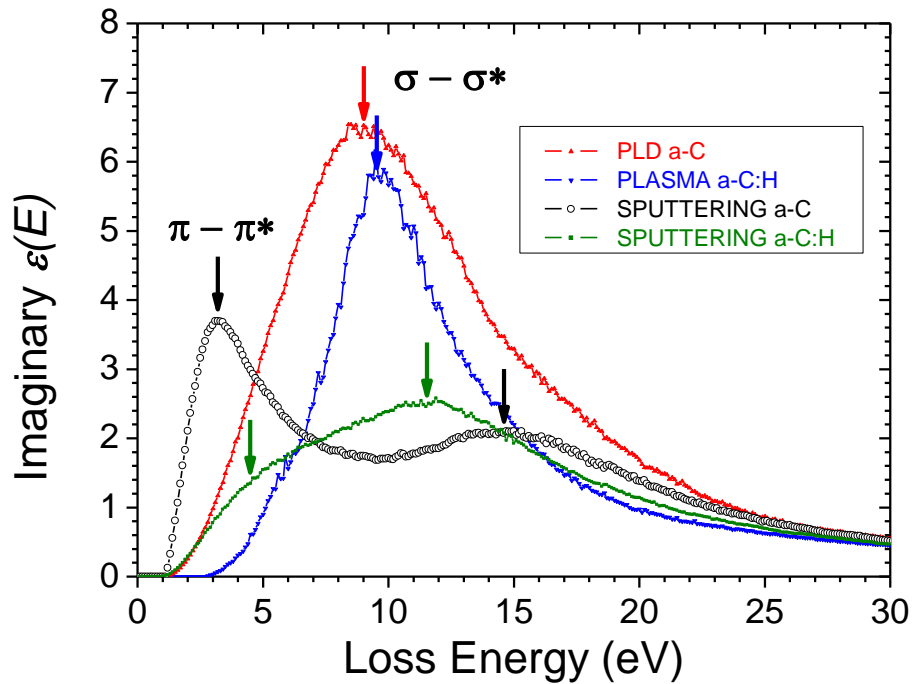


**Fig. 8.** Imaginary part of the dielectric function  $\varepsilon(E)$  of a-C surfaces derived from PEELS analysis: a-C (PLD), a-C:H (SP), a-C (SP) and aC (PL) using  $n(E \approx 0)$  values given in **Table I**.

Consistently, very different dielectric functions are retrieved for the four amorphous carbon films (**Fig. 8**). The imaginary part of the dielectric function of the  $sp^2$ -rich sputtered a-C shows two broad

peaks which are likely attributed to  $\pi$ - $\pi^*$  transitions (3.5 eV) and to  $\sigma$ - $\sigma^*$  transitions ( $15 \pm 1$  eV). In contrast, the plasma-deposited a-C:H film with small  $sp^2$  C content and wide band gap ( $E_T \approx 2.5$  eV) essentially shows a narrow  $\sigma$ - $\sigma^*$  peak at 9.5 eV. Interestingly, in the low-density  $sp^2$ -rich sputtered a-C:H ( $E_P = 26.5$  eV) and in the high-density PLD a-C ( $E_P = 31$  eV) films,  $\pi$ - $\pi^*$  and  $\sigma$ - $\sigma^*$  transitions have nearly merged into a broad peak, extending from 5 eV to 15 eV at half maximum. Finally, the  $\sigma$ - $\sigma^*$  transition energy increases from 9.5 eV to 15 eV, as the  $sp^2$  hybridization increases.

## 5. DISCUSSION

The inversion algorithm for XPS-PEELS data analysis is discussed in terms of four output parameters summarized in **Table II** : (i) the complex dielectric function,  $\epsilon(\hbar\omega)$ , of the near-surface material, obtained over a very broad energy range, is compared to bulk optical (e.g. ellipsometry) data in the near-UV to visible range and previous EELS characterizations; (ii) the IMFP,  $\lambda_P(E_0)$ , values for plasmon losses is compared with literature data for carbon allotropes obtained using independent optical and Elastic peak electron spectroscopy (EPES) data; (iii) the effective number of valence electrons per atom participating in plasma oscillation is given by the  $f$ -sum rules; (iv) the surface plasmon loss distribution and surface excitation probability are evaluated at normal emission angle.

Note that Born-Bethe sensitivity factors,  $f(\hbar\omega)$  and  $g(\hbar\omega, \alpha)$ , respectively for bulk and surface loss distributions are required for the recovery of the primary bulk plasmon loss  $S_B(\hbar\omega)/f(\hbar\omega)$ , and surface plasmon loss  $S_s(\hbar\omega)/g(\hbar\omega, \alpha)$ . This correction is also important for the determination of the Inelastic Mean Free Path value and the dielectric function. The uncertainties arising from possible errors in the surface refractive index  $n(E \approx 0)$ , weighting function (exponential vs polynomial) or data fitting at low loss energy, power-law extrapolation function (exponent) will be tentatively addressed and a comparison will be made between a-C, a-C:H and previously reported PEELS data for a-Si:H [26].

### 5.1. Dielectric function

The accuracy and reproducibility of data treatment depends primarily on the quality of photoemission peak removal. For ta-C and a-C:H films with a large bandgap energy value and dominated by  $\sigma$ - $\sigma^*$  transitions, robust results have been obtained since all methods provide essentially similar ELF and dielectric function. In contrast, for low bandgap carbon films, e.g. sputtered a-C, great care must be taken to separate the quasi-elastic peak from low energy losses. In this study, we have first fitted low energy losses with an empirical analytical function, and in a second step adjusted the width of the sigmoid weighting function to remove spurious signal.

This algorithm provides reliable information near the core level peak but energy losses smaller than 1 eV remain beyond the capability of the method. For all films, fair agreement is found between the real and imaginary parts of the dielectric function, retrieved from PEELS data, and ellipsometry data in the UV-visible range (not shown). Since the dielectric function peaks depend strongly on the precise determination of refractive index independently measured at low energy [43], some limitation of the method could result from the limited energy range of ellipsometry data (0.7-4.5 eV), however, for semiconductors  $\text{Re}(1/\epsilon)$  is rather flat at low energy and extrapolation below 0.7 eV is very safe; in contrast, if a strong Drude component is present at low energy (metal or semi metallic material), **Eqn. C3** should be normalized to 1.

The dielectric function changes strongly as a function of the  $\text{sp}^2$ - $\text{sp}^3$  hybridization, as expected, but also with the incorporation of hydrogen, both in the spectral weight of  $\pi$ - $\pi^*$  transitions below 7 eV and in the position or width of  $\sigma$ - $\sigma^*$  transitions.

Let us first consider  $\text{sp}^3$ -rich carbon films: the  $\sigma$ - $\sigma^*$  peak energy in both plasma a-C:H and PLD a-C ( $\approx 9.5$  eV) is lower than in diamond (12.3 eV) because of the loss of the  $k$ -selection rule in disordered solids [43]. In the region of  $\sigma$ - $\sigma^*$  transitions, the dielectric function observed in  $\text{sp}^3$ -rich PLD a-C is very broad as compared with the plasma-grown a-C:H. This is expected from the larger  $\text{sp}^2$ -content in PLD a-C since the  $\sigma$ - $\sigma^*$  peak is the superposition of  $\sigma$ - $\sigma^*$  transitions at  $\text{sp}^2$  sites and  $\sigma$ - $\sigma^*$  transitions at  $\text{sp}^3$  sites, which cannot be separated. In addition, local constraints may result from high atom density in PLD a-C whereas dihedral angle relaxation may be allowed by hydrogen incorporation in a-C:H. Interestingly, the dielectric function retrieved from our PEELS data (e.g.  $\epsilon_{2\text{MAX}} = 6.5$  at  $\epsilon_2$  peak maximum,  $\sigma$ - $\sigma^*$  peak at 9.0 eV and full width  $\approx 10$  eV) for  $\text{sp}^3$ -rich PLD a-C coincides with  $\epsilon(E)$  derived from TEELS data for tetrahedral amorphous carbon (ta-C) grown by the filtered cathodic arc technique ( $2.9 \text{ g.cm}^{-3}$ ,  $E_P = 30$  eV) [15].

Considering  $\text{sp}^2$ -rich sputtered amorphous carbons, unexpected difference is found between the broad dielectric function of a-C:H where  $\pi$ - $\pi^*$  and  $\sigma$ - $\sigma^*$  transitions have nearly merged, and the well-separated peaks found in nominally hydrogen-free a-C, i.e.  $\pi$ - $\pi^*$  transitions near 3.5 eV and a broad distribution of  $\sigma$ - $\sigma^*$  transitions centred at 15 eV. The latter reminds of the  $\epsilon_2(E)$  spectrum of graphite for in-plane polarization [44] and that of arc-evaporated a-C ( $1.90 \text{ g.cm}^{-3}$ ) [45]; the presence of a  $\pi$  plasmon at 6.5 eV (**Fig. 7**) indicates that some ordered  $\text{sp}^2$ -bonding is present in sputtered a-C; however, there is no clear plateau near 8 eV in  $N_{\text{EFF}}(T)$  to mark a separation between  $\pi$ - $\pi^*$  and  $\sigma$ - $\sigma^*$  transitions as found in graphite. This is taken as some indication that the disordered structure is responsible for some s-p hybridization of the  $\pi$  states [46] and hence for  $\sigma$ - $\pi$  orbital mixing related to

local constraints in amorphous carbon [15, 47, 48]. The effect is even stronger in sputtered a-C:H, where the signature of  $\pi$ - $\pi^*$  transitions has a very small spectral weight in spite of a large  $sp^2$  C hybridization as observed in XPS.

It is interesting to note that the  $\sigma$ - $\sigma^*$  transition energy increases from 9.5 eV to 15 eV, as the  $sp^2$  hybridization increases, in rather good agreement with optical data measured in a narrow energy range and analysed using two Tauc-Lorentz oscillators [49].

## 5.2. Inelastic mean free path

The IMFP of electrons crossing a solid is an important parameter to calibrate the length scale and to evaluate background spectra in photoelectron spectroscopies. However, the accurate determination of the average distance an electron travels between successive inelastic collisions, measured along its flight path, is not straightforward [50]. The algorithm results presented here are compared with previous methods by considering physical hypothesis made in the respective models.

Elastic peak electron spectroscopy is considered as a reliable technique for measurements of IMFP, in contrast with the overlayer method [50, 51] which rather provides the attenuation length. In EPES, the elastic reflection coefficient of electrons backscattered from a solid surface depends linearly on the IMFP [50, 52].

Another method to obtain IMFP values is based on an analysis of optical measurements, usually selected according to the  $f$ -sum rule criterion for internal consistency, and it exclusively relies on dielectric theory [53-55]. Linear response theory is used to extrapolate the  $(\omega, q=0)$  optical loss function to non-vanishing momentum transfers in the  $(\omega, q)$  plane [56]. The calculated  $\lambda_P(E_0)$  values can be fitted by a modified Bethe equation for inelastic electron scattering [57] and an empirical predictive formula designated as TPP-2M was proposed to obtain IMFP values in other materials [58, 59]. For  $E_0$  values above 200 eV, it reduces to the equation  $(E_0 / \lambda_P) = \beta E_P^2 \text{Ln}(\gamma E_0)$ , with  $\beta$  and  $\gamma$  parameters extracted from the linear part of the Fano plot, i.e.  $(E_0 / \lambda_P)$  vs.  $\text{Ln}(E_0)$ . Note that for the allotropes of carbon (diamond, graphite, glassy carbon), the IMFPs derived from the TPP-2M equation have a large standard uncertainty due to the very small  $\beta$  parameter value [55].

In this work, the Inelastic Mean Free Path,  $\lambda_P(E_0)$ , value corresponding to plasmon losses has been derived from PEELS data using the sensitivity factor  $f_C(\hbar\omega)$  (**Eq. (A.6)**) as illustrated here for C 1s and Si 2p core levels. As the atom density of amorphous carbon decreases, in the series a-C (PLD) > a-C (PL) > a-C (SP) > a-C:H (SP) as derived from the  $N_{\text{EFF}}$  plateau value, the IMFP for plasmon losses,  $\lambda_P(970 \text{ eV})$ , obtained from PEELS analysis increases from 1.22 nm to 1.60 nm (**Table II**).

Comparison of these PEELS results with available IMFP data from the literature deserves several comments:

- For the dense  $sp^3$ -rich PLD a-C, the experimental value of  $\lambda_P(970 \text{ eV}) = 1.22 \text{ nm}$  is smaller than both IMFP for nanocrystalline diamond (95 %  $sp^3$ ) obtained from EPES,  $\lambda_{EPES}(970 \text{ eV}) = 1.5 \text{ nm}$  [60] and TPP-2M predicted value  $\approx 1.5 \text{ nm}$  [61].
- For the  $sp^2$ -rich sputtered a-C:H / a-C surfaces, experimental values of  $\lambda_P(970 \text{ eV}) = 1.60 / 1.50 \text{ nm}$  are smaller than the value  $\lambda_{OPT}(970 \text{ eV}) = 2.06 \text{ nm} / 1.64 \text{ nm}$  calculated using  $E_P = 25 \text{ eV} / 28 \text{ eV}$  and the parameters ( $\beta = 0.0159 \text{ eV}^{-1} \text{ \AA}^{-1}$ ,  $\gamma = 0.117 \text{ eV}^{-1}$ ) adjusted to the optical data for glassy carbon [55]; the discrepancy is slightly larger if one considers the values  $\lambda_{EPES}(970 \text{ eV}) = \mathbf{2.24 \text{ nm} / 1.79 \text{ nm}}$  calculated using parameters ( $\beta = 0.015 \text{ eV}^{-1} \text{ \AA}^{-1}$ ,  $\gamma = 0.104 \text{ eV}^{-1}$ ) adjusted to EPES data for ion-bombarded carbon [52].
- For amorphous silicon a-Si:H, the experimental value of  $\lambda_P(1154 \text{ eV}) = 1.9 \text{ nm}$  is smaller than both values of  $\lambda_{OPT}(1154 \text{ eV}) = 2.70 \text{ nm}$  obtained from optical data [59] and  $\lambda_{EPES}(1154 \text{ eV}) = 2.75 \text{ nm}$  calculated using  $E_P = 17 \text{ eV}$  and the parameters ( $\beta = 0.039 \text{ eV}^{-1} \text{ \AA}^{-1}$ ,  $\gamma = 0.036 \text{ eV}^{-1}$ ) adjusted to EPES data for crystalline silicon [51].

**Table II** : Atom density ( $N_{AT} = N_{EFF}/4$ ), plasmon energies  $E_P$  and  $E_P^0$ , SEP and parameter  $a$ , inelastic mean free path,  $\lambda_P$ , derived from XPS-PEELS (this work, using a Free Electron model of the cutoff wave vector) as compared with previous estimates,  $\lambda_{P \text{ CALC}}$ , for MgK $\alpha$  excited C1s ( $E_0 = 970 \text{ eV}$ ) and Si2p ( $E_0 = 1154 \text{ eV}$ ) core levels: (\*) optical data (R2 [59], R3 [55]), (\*\*) EPES data (R1 [52]).

Material sp <sup>3</sup> %	$N_{AT} = N_{EFF}/4$ (10 <sup>22</sup> at.cm <sup>-3</sup> )	$E_P^0$ (eV)	$E_P$ (eV)	SEP ( $E_0$ ) $a$ ( $E_0$ )	$\lambda_{P \text{ EXP}}(E_0)$ nm	$\lambda_{P \text{ CALC}}(E_0)$ nm	Ref.
a-Si:H Plasma	<b>5.0</b>	<b>16.6</b>	<b>17.0</b>		1.90	<b>2.75</b> <b>2.70</b>	R1 R2
a-C:H Plasma	<b>10.3</b>	<b>21.8</b>	<b>24.0</b>	0.071 <b>2.4</b>	1.45	<b>2.77</b> <b>2.55</b>	R1 R3
a-C PLD	<b>14.5</b>	<b>29.3</b>	<b>31.0</b>	0.079 <b>2.2</b>	1.22	<b>1.56</b> <b>1.43</b>	R1 R3
a-C Sputtered	<b>9.9</b>	<b>26.1</b>	<b>28.0</b>	0.104 <b>1.6</b>	1.50	<b>2.07</b> <b>1.91</b>	R1 R3
a-C:H Sputtered	<b>9.3</b>	<b>24.5</b>	<b>26.5</b>	0.089 <b>1.9</b>	1.60	<b>2.07</b> <b>1.91</b>	R1 R3

Taken together, results reported in **Table II** reveal a systematic underestimation, by 30% to 80%, of the IMFP values for plasmon excitation derived from this XPS-PEELS analysis as compared with tabulated IMFP references, both for a-C films with variable hybridization and for the well-characterized device-grade a-Si:H. Factors affecting the accuracy of the determination of the IMFP have been discussed in the literature [50]. Systematic errors may arise in XPS-PEELS analysis:

(i) if the surface refractive index is smaller than the SE measured bulk value, **Eq. (C.10)** shows that  $\lambda_P$  can be slightly underestimated, however this hypothesis is unlikely since it would require differences larger than 40% between surface and bulk refractive index values of a-C.

(ii) if electrons with the same source location do not travel identical path lengths in the solid as a consequence of elastic scattering; here the IMFP,  $\lambda_P(970 \text{ eV}) = 1.22 \text{ nm}$ , for a-C (PLD) is very similar to the elastic mean free path,  $\lambda_E(970 \text{ eV}) = 1.28 \text{ nm}$ , calculated using  $\sigma_E(970 \text{ eV}) = 1.99 a_0^2$  [62] and the XRR atom density. Since elastic collisions at photoelectron energies near 1 keV are strongly peaked in the forward direction, they can be reasonably neglected for XPS-PEELS analysis of a-C; hence the energy loss distribution is well described by convolution of the energy loss distribution in a single collision [19]. This conclusion is also valid for a-Si:H where  $\sigma_E(1154 \text{ eV}) = 4.45 a_0^2$  and  $\lambda_E(1154 \text{ eV}) = 1.60 \text{ nm}$ .

(iii) in order to obtain the Born-Bethe factor, Calliari *et al.* [63] have recently proposed to use the Bethe ridge angle  $\theta_B$  (which represents the energy loss of an electron scattered by an electron at rest) rather than the cutoff angle  $\theta_C$  given by the free electron model. For Si, this correction at  $E_P$  value would increase the calculated IMFP by 21 % (from 2.1 to 2.54 nm) while for PLD a-C, this correction would increase the calculated IMFP by 37 % (from 1.22 to 1.69 nm). However, this approach would also change the retrieved dielectric function.

Conversely, setting the IMFP to the tabulated value requires an increase of the effective  $q_C$  value as compared with the theoretical one obtained with the Free Electron (FE) model. More work is required to understand if this is due to dispersion effects (deviation of the approximation  $\eta \approx 0.5$  in **Appendix B**) or from band structure effects.

### 5.3. Sum rules

In order to apply sum rules, the atom density  $N_{AT}$  is needed to obtain the effective number  $N_{EFF}$  of electrons per atom participating in the  $(\sigma+\pi)$  plasma oscillation (**Appendix C**). Independent measurement of the atom density averaged over film thickness can be derived either from the optical

index  $n(0)$  and effective medium theory (using a reference material with identical composition) or from modeling X-ray reflectometry (XRR) data.

For PLD a-C, the mass density  $\rho_C$  is known precisely from XRR measurements taken as a function of grazing incidence angle in a  $\theta - 2\theta$  scan [39, 49, 64]. Almost all information about the investigated material is related with the electron density distribution,  $\rho(r)$ . The atom density  $\rho_C$  of a-C films grown on c-Si is related to the critical angle  $\xi_C$  for total external reflection:

$$\xi_C^2 = (e^2 \lambda^2 / \pi m_0 c^2) (N_0 Z / A) \rho_C \quad (6)$$

where  $N_0$  is the Avogadro number,  $Z$  and  $A$  are the atomic number and molar mass,  $e$  and  $m_0$  are the electron charge and mass,  $\lambda$  is the X-ray wavelength and  $c$  is the light velocity in air. For PLD a-C,  $\rho_C = 2.84 \pm 0.05 \text{ g.cm}^{-3}$  and the atom density is  $N_C = (N_0 / A) \rho_C = 1.42 \cdot 10^{23} \text{ cm}^{-3}$ , in good agreement with a well-established correlation between atom density and  $(sp^3 / sp^2 + sp^3)$  ratio [49, 64, 65]. Using the atom density obtained independently from XRR, two consequences can be drawn for PLD a-C.

On the one hand, in the FE model, plasmon energy  $E_p^0 = 28.8(N_V \rho_C / A)^{1/2}$  is expected at  $E_p^0 = 28.0 \text{ eV}$  if effective number of valence electrons  $N_V = 4$  is assumed. In a Drude-Lorentz model useful for semiconductors, the free-electron plasmon energy,  $E_p^0$ , is smaller than the observed plasmon energy  $E_p$  [64] given by  $E_p^2 = E_{p_0}^2 + E_{PG}^2$ , where  $E_{PG}$  is the Penn gap i.e. the average bonding-antibonding splitting; in PLD a-C, we thus expect  $E_p = 29.7 \text{ eV}$ , using  $E_{PG} = 10 \text{ eV}$  (Fig. 8). Similarly, since the density of device-grade a-Si:H, derived from optical measurements, [66] is within a few percent of the crystalline phase ( $\rho_{Si} = 2.33 \text{ g.cm}^{-3}$  and  $N_{Si} = 0.50 \cdot 10^{23} \text{ cm}^{-3}$ ) we expect to find  $E_p^0 = 16.6 \text{ eV}$  and  $E_p = 17.0 \text{ eV}$  (using  $E_{PG} = 3.5 \text{ eV}$ ). In both cases, predictions are quite close to experiments.

On the other hand, the effective number,  $N_{\text{EFF}}$ , of valence electrons active in plasmon oscillation, obtained from the  $f$ -sum rules near 100 eV (Appendix C), is close to  $N_{\text{EFF}} = 4.0 \pm 0.1$  for a-C (PLD), which indicates a good accuracy of the optical  $\epsilon(\hbar\omega = 0)$  value. Conversely, calibration of  $N_{\text{AT}}$  can be obtained by arbitrarily setting  $N_{\text{EFF}} = 4$  for the  $(\sigma + \pi)$  plasmon in all amorphous carbon surfaces, the resulting atom density value increases from  $0.93 \cdot 10^{23}$  to  $1.45 \cdot 10^{23} \text{ at.cm}^{-3}$  (Table II).

#### 5.4. Surface plasmon losses

Angular measurements of core level loss spectra are useful to identify properly the energy distribution and probability of surface plasmon excitations. This work shows that surface and bulk plasmon energy distributions can be constrained to be self-consistent, i.e. to correspond to the same

dielectric function. The relative SEP variation for a-C surfaces is described by the expected ( $b / \cos\alpha$ ) dependence, which confirms previous angular XPS studies [17]. A similar angular dependence and stronger SEP are observed for surface modification of a-C with dense organic monolayer.

For surface plasmon excitation, the interaction depth is a few monolayers thick and usually provides at most single surface plasmon scattering, unless photoelectron take-off angle is very small. The effective region extends into the solid to a depth about  $\sim (v / 2\omega_S)$ , [2-4, 11, 33] where  $\omega_S$  is the surface plasmon frequency and  $v$  the photoelectron velocity. For MgK $\alpha$  X-rays (1453.6 eV), since  $\omega_S \approx 21$  eV, this depth is  $\delta_S \approx 0.3$  nm in a-C PLD while for a-Si:H  $\omega_S \approx 12$  eV and  $\delta_S \approx 0.55$  nm. Hence, the IMFP value derived from XPS-PEELS analysis with FE model is  $\lambda_P(E_0) \approx 4\delta_S(E_0)$  for both amorphous materials.

The SEP value (Eq. 4) is the ratio of the integrated  $S_S(T)$  distribution (Fig. C.1) to the integrated photoemission peak,  $J(T)[1-\sigma(T)]$ . For PLD a-C,  $P_S = 0.08$  gives  $a = 2.2 \pm 0.2$ , which confirms a previous estimate  $a = 2 \pm 0.5$  [17]. In the experimental range of parameter  $a$  values, between 1.6 and 2.4 (Table II) found for disordered carbons, Pauly's model, [32]  $a_P = 0.016E_P + 0.82 + 0.27E_G$ , provides better matching than earlier Werner's model, [31]  $a_W = 0.139E_P + 0.4$ . Our results indicate some positive correlation between  $E_P$  and parameter  $a$  (the slope being about twice that given in Pauly's model) but more SEP data would be required to draw conclusions. It has been argued that lower  $P_S$  values are expected for XPS due to the presence of the core hole [22]. A positive correlation appears between parameter  $a$  and  $sp^3$ -hybridization of the carbon surface. Our results are consistent with the fact that surface excitation principally arises at small energies and the presence of an energy gap effectively reduces the range of channels for these excitations [67].

## 6. CONCLUSIONS

The near-surface dielectric function  $\epsilon(\hbar\omega)$  and inelastic mean free path of C1s photoelectrons in a-C films with different ( $sp^3 / sp^2+sp^3$ ) C hybridization have been derived from experimental energy-loss distribution in XPS spectra, using a dielectric response theory which relates  $\epsilon(\hbar\omega)$  and the single loss distribution  $S_B(T)$  due to collective electron oscillations. Energy loss spectra are readily obtained from any laboratory XP spectrometer (without demanding synchrotron environment), although a compromise must be found between energy resolution and signal-to-noise ratio.

In order to keep as much as possible of the spectroscopic information contained in XPS-PEELS data, several methods (weighting function vs subtraction of fitted analytic function) have been compared

and combined to eliminate the photoemission peak tailing at low loss energy due to many-body interactions during core level photoionization, without introducing spurious signal or additional noise. The fact that the most widely used and physically sound asymmetrical line shape (as proposed by Doniach-Sunjic) does not give satisfactory results will be addressed in a separate publication.

This inversion algorithm has been applied to smooth a-C and a-C:H surfaces grown using different techniques to get a wide range of physical properties (atom density,  $sp^2$ - $sp^3$  hybridization). Reliable information on the ELF is retrieved near the core level peak but energy losses smaller than 1 eV remain beyond the capability of the method. The IMFP being nearly equal to the elastic mean free path in a-C films, the energy loss distribution is accurately described in terms of a convolution of the energy loss distribution in a single scattering event. The retrieved dielectric function for  $sp^3$ -rich PLD a-C coincides with  $\epsilon(E)$  derived from TEELS for tetrahedral amorphous carbon while that of  $sp^2$ -rich sputtered a-C reminds of arc-evaporated a-C with the presence of a  $\pi$  plasmon at 6.5 eV indicating some ordered  $sp^2$ -bonding. In sputtered a-C:H,  $\sigma$ - $\pi$  orbital mixing is attributed to local constraints in the disordered structure. In summary, dielectric function results show that electronic properties of disordered carbons can hardly be described by a single parameter, e.g. the average ( $sp^3 / sp^2+sp^3$ ) hybridization, because additional complexity is brought by medium range organization of  $sp^2$ -bonded clusters and by the presence of both  $\pi$ - $\pi^*$  and  $\sigma$ - $\sigma^*$  transitions.

As the C atom density of amorphous carbon decreases, in the series a-C (PLD) > a-C:H (SP) > a-C:H (PL) > a-C (SP) as derived from the sum rule giving  $N_{EFF}$ , the IMFP for plasmon losses,  $\lambda_P$  (970 eV), obtained from XPS-PEELS analysis increases from 1.22 nm to 1.6 nm using a Free Electron model of the cutoff wave vector; the latter results are smaller than values provided by predictive formulae (e.g. TPP-2M) beyond the standard uncertainty found for carbon allotropes [55]. Since IMFP absolute values depend on the accurate definition of a cutoff wave number through the Born-Bethe sensitivity factor, further investigations will be useful to elucidate why the Bethe ridge angle  $\theta_B = (E_P / E_0)^{1/2}$  apparently gives more consistent values than the cutoff angle  $\theta_C$  given by the FE model; dispersion effects which were neglected in this study might also be considered in the Born-Bethe factor [63].

Besides simple mathematical improvements, such as derivation of plasmon loss spectra in the case of doublet core levels, more fundamental developments can be expected from a comprehensive use of optical measurements to strengthen the normalization of the single plasmon loss signal. This method opens new horizons in the field of material research because it can be applied to any material that presents strong and isolated XPS lines with a neat plasmon loss spectrum. Interesting electronic

properties of oxides and nitrides [68, 69] have been studied by XPS-PEELS in a wide energy range (UV, VUV) that is actually difficult to explore by optical methods.

### **Acknowledgments**

One of us (C.G.) is grateful to CNPq agency for a visiting researcher grant (PVE 400691/2012-4) in the *Ciência Sem Fronteiras* programme. One of us (D.D.) is grateful to CAPES agency (Brazil) for a senior researcher grant and University of Rennes 1 for an invited professor position. The authors acknowledge Kacem Zellama (LPMC, Amiens University) for sputtered a-C films, João Pedro Conde and Virginia Chu (INESC-MN, Lisbon) for plasma deposition of a-C:H films, Stéphanie Députier, André Perrin and Maryline Guilloux-Viry (LCSIM, Rennes University) for pulsed laser deposition of a-C films, Bruno Fabre (MaCSE, Rennes University) and Hussein Sabbah (IPR, Rennes University) for molecular grafting experiments. This work also benefited from theoretical discussions with Prof. Jailton de Almeida and Prof. Antônio Ferreira da Silva (UFBa, Brazil).

## Appendix A: Determination of Bethe-Born factors

In contrast with the monokinetic electron beam used in EELS / REELS, XPS photoelectrons result from photo-ionization of atoms by X-ray photons, with a cross section which depends on the angle  $\gamma$  between photon and electron directions [70, 71].

In addition, bulk and surface inelastic cross-sections  $\sigma_{in}$  show some dependence on the scattering angle  $\theta$  [3 Egerton]. Since kinetic energy loss,  $T$ , and scattering angle,  $\theta$ , are linked through the energy and momentum conservation rules, a sensitivity factor or Bethe-Born factor  $f(T)$  affects the measured ELF for bulk plasmon excitation. A similar effect given by a sensitivity function  $g(T)$  occurs for surface plasmon excitation. Hence, the measured XPS-PEELS signal must be divided by bulk and surface sensitivity factors, respectively  $f(T)$  and  $g(T)$ , calculated below by averaging over scattering direction.

As far as the dependence of sensitivity factors on loss energy is concerned, elastic scattering will be neglected, although angular deflections contribute to increase the electron path length before escaping the solid. For C atoms, the differential cross section is strongly peaked in the forward direction and the elastic cross section is  $\sigma_E = 1.986 a_0^2$  [62].

### 1. Angular dependence of the photo-ionization cross section

We assume a uniform distribution of emission depths in the surface region since the attenuation of X-rays in solids is much smaller than the attenuation of electrons. The angular distribution of these electrons is determined by the differential photoionization cross section. In the electric dipole approximation (neglecting quadrupolar effects), the ionization of an  $nl$  subshell by unpolarized X-rays is given by [71]:

$$\frac{d\sigma_{nl}}{d\Omega} = \frac{\sigma_{nl}(E)}{4\pi} \cdot \left(1 - \frac{1}{4}\beta_{nl}(3\cos^2\gamma - 1)\right) \quad (\text{A.1})$$

where  $\sigma_{nl}(E)$  is the total photoelectric cross-section,  $\gamma$  is the angle between the incident photons and emitted photoelectrons, and  $\beta_{nl}$  is the subshell asymmetry parameter:  $\beta_{nl}(\text{C } 1s) = 2$ ,  $\beta_{nl}(\text{Si } 2p) \approx 1.1$ . Small corrections on the angular term result from elastic collisions [62]. For electrons going out of the material without any scattering, if  $\gamma = \gamma_0 = 54.7^\circ$  (as in many XPS systems), the cross section is independent of  $\beta_{nl}$ :

$$\frac{d\sigma_{nl}}{d\Omega} = \frac{\sigma_{nl}(E)}{4\pi} \quad (\text{A.2})$$

Hence for an isotropic amorphous solid (without photo-diffraction effects), the measured photoemission peak shows no angular dependence due to the photo-ionization cross-section.

## 2. Dependence of $f_C(T)$ for bulk plasmon excitation

Energy and momentum conservation rules applied to inelastic scattering of a photoelectron from  $(E_0, k_0)$  to  $(E_1, k_1)$ , where  $E_1 = E_0 - T$  and  $\theta = (\vec{k}_0, \vec{k}_1)$ , provide the wave vector  $\vec{q} = \vec{k}_0 - \vec{k}_1$ :

$$q^2 = 2k_0^2 \left[ 1 - \theta_T - (1 - 2\theta_T)^{1/2} \cos \theta \right] \quad \text{with } \theta_T(T) = T / 2E_0 \quad (\text{A.3})$$

The scattered photo-electrons entering the analyzer, after a single inelastic scattering event, are defined by  $\cos \theta = \cos \gamma \cos \gamma_0 + \sin \gamma \sin \gamma_0 \cos \phi$ , where  $\gamma_0$  is the angle between X-ray direction and spectrometer axis,  $\gamma$  and  $\phi$  are respectively the zenithal and azimuthal angles of emission of the photo-electron. For small  $\theta$  values, the approximation  $\gamma = \gamma_0$  holds and  $0 < \phi < 2\pi$ .

The differential inverse inelastic mean free path (DIIMFP) is [3]

$$K(E_0, T) = \oint \frac{d^2 \sigma_{\text{in}}}{d\Omega dT} d\Omega = \oint \left( \frac{k_0^2}{\pi^2 a_0 m_0 v^2 q^2} \right) \text{Im} \left( -\frac{1}{\varepsilon(T, q)} \right) d\Omega \quad (\text{A.4})$$

where  $m$  and  $v$  are respectively the mass and the velocity of primary photoelectrons,  $\varepsilon(T)$  is the dielectric function of the material,  $a_0$  is the Bohr radius. Integration over the solid angle  $d\Omega = 2\pi \sin \theta d\theta \approx 2\pi k_0^{-2} q_{\perp} dq_{\perp}$  gives :

$$K(E_0, T) = \int_{q^-}^{q^+} \frac{1}{2\pi^2 a_0 E_0} \text{Im} \left( -\frac{1}{\varepsilon(T, q)} \right) \frac{2\pi \sin \theta d\theta}{(\theta^2 + \theta_T^2)} \quad (\text{A.5})$$

where kinematic limits  $q_{\pm} = (2m / \hbar^2)^{1/2} [E_0^{1/2} \pm (E_0 - T)^{1/2}]$  have been considered. As a matter of fact, the physics of plasmon excitation [2] requires additional constraint over  $q$  values, because plasma oscillations are strongly damped above a critical (material dependent) wave vector  $q_C$  ( $q_C < q^+$ ) defined in the FE model (**Appendix B**). Hence, the Bethe-Born sensitivity factor  $f_C(T)$  writes:

$$f_C(T) = 2\pi \int_0^{q_C} \frac{\theta d\theta}{\theta^2 + (\theta_T)^2} = \pi \text{Ln} \left( \left( \frac{\theta_C}{\theta_T} \right)^2 + 1 \right) \quad (\text{A.6})$$

which depends on  $\theta_T(T)$  and  $\theta_C = \cos^{-1} \left[ \frac{1 - \theta_T - (q_C^2 / 2k_0^2)}{(1 - 2\theta_T)^{1/2}} \right] \approx \frac{q_C}{k_0}$  for small  $\theta_T(T)$ . Hence:

$$K(E_0, T) = \frac{1}{2\pi^2 a_0 E_0} \text{Im} \left( -\frac{1}{\varepsilon(T, q)} \right) \pi \text{Ln} \left[ 1 + \left( \frac{\theta_C}{\theta_T} \right)^2 \right] \quad (\text{A.7})$$

In contrast, the (unphysical) integration over the whole space ( $4\pi$  sr) results in a function  $f_A(T) > f_C(T)$ :

$$f_A(T) = \pi \text{Ln} \left( \frac{A(T)+1}{A(T)-1} \right) \quad \text{with} \quad A(T) = \left( 1 - \frac{T}{2E_0} \right) \left( 1 - \frac{T}{E_0} \right)^{\frac{1}{2}} \quad (\text{A.8})$$

Using **Eq (A.6)**, the inverse inelastic mean free path (IIMFP) is obtained :

$$\frac{1}{\lambda_p} = \int_0^{E_{MAX}} K(E_0, T) dT = \int_0^{\infty} \frac{f_C(T)}{2\pi^2 a_0 E_0} \text{Im} \left( -\frac{1}{\varepsilon(T)} \right) dT \quad (\text{A.9})$$

Sensitivity factors  $f_C(T)$  and  $f_A(T)$  were calculated for the C(1s) core level with MgK $\alpha$  excitation (**Fig. A.1**). Since photoelectrons scattered with low loss-energy have higher sensitivity, application of this correction in **step 5** of the algorithm reinforces the high energy loss part of the spectrum and results in a small displacement of the plasmon peak toward higher loss energy.

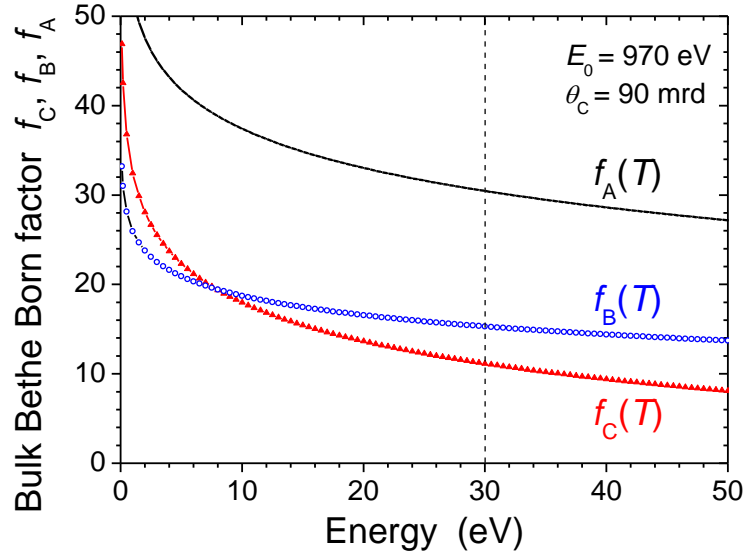


**Fig. A.1:** Sensitivity factors for volume inelastic scattering of C1s photoelectrons ( $E_0 = 970$  eV).  $f_C(T)$ ,  $f_B(T)$  are obtained from **Eq. (A6)** using respectively a free electron model ( $\theta_C = 90$  mrd) or the Bethe ridge angle ( $\theta_B$ ) while  $f_A(T)$  is given by **Eq. (A8)**.

### 3. Dependence of $g(T, \alpha)$ for surface plasmon excitation

Photoelectrons with initial velocity  $v$  and momentum  $k_0$  crossing a planar boundary can lose energy with probability [3]:

$$\frac{d^2 P}{d\Omega \cdot dE} = \frac{k_0^2 |q_s|}{\pi^2 a_0 m_0 v^2 q^4 \cos \theta_i} \cdot \text{Im} \left( \frac{(\varepsilon_a - \varepsilon_b)^2}{\varepsilon_a \varepsilon_b (\varepsilon_a + \varepsilon_b)} \right) \quad (\text{A.10})$$

where  $\vec{q}_s$  is the projection of vector  $\vec{q} = \vec{k}_0 - \vec{k}_1$  onto the boundary plane  $S$  (**Fig. A.2**).

In XPS experiments with planar material / vacuum boundary,  $\varepsilon_a = \varepsilon$  and  $\varepsilon_b = 1$ :

$$\text{Im}\left(\frac{(\varepsilon_a - \varepsilon_b)^2}{\varepsilon_a \varepsilon_b (\varepsilon_a + \varepsilon_b)}\right) = \text{Im}\left(\frac{1}{\varepsilon} - \frac{4}{1 + \varepsilon}\right) \quad (\text{A.11})$$

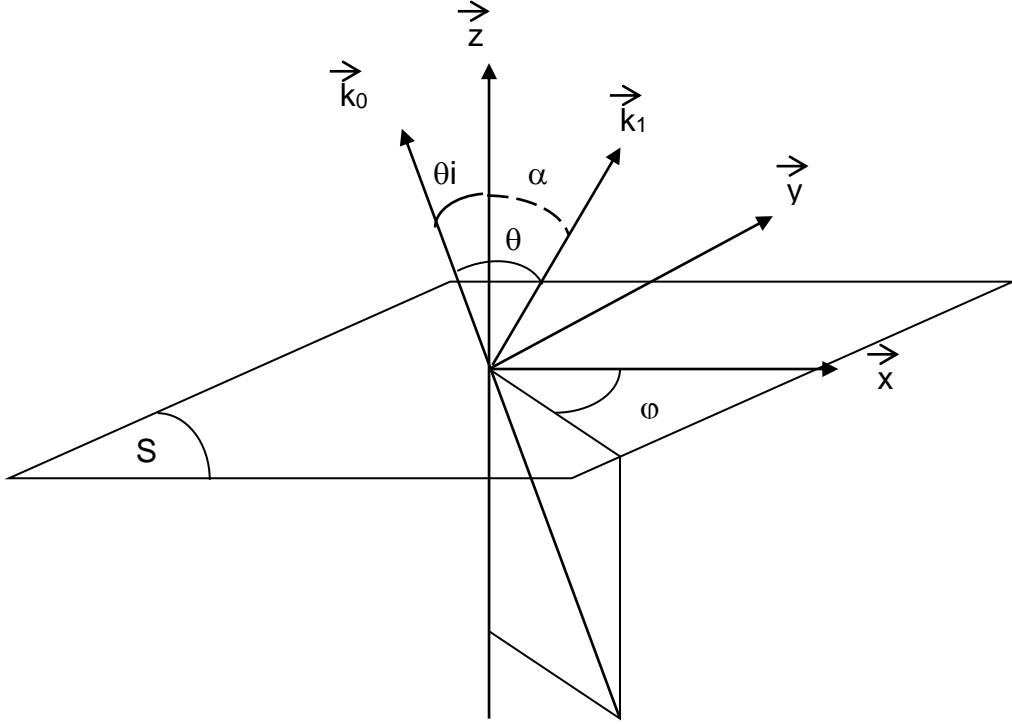


**Fig. A.2:** Angles involved in the surface scattering ( $k_0$  incident electron,  $k_1$  scattered electron).

We define  $\theta_i$  the zenithal angle between the incident wave vector  $k_0$  and the normal to the surface,  $\phi$  the azimuthal angle and  $\alpha$  the angle between the normal to the surface, and the spectrometer axis (**Fig. A.2**). The scattering angle  $\theta$  is given by  $\cos\theta = \sin\alpha \cdot \sin\theta_i \cdot \cos\phi + \cos\alpha \cdot \cos\theta_i$ . Using **Eq. (A3)**, we can express  $|q_s|$  and  $q^4$  as a function of scattering angle  $\theta$  and energy loss  $T$ :

$$|\vec{q}_s| = k_0 \sqrt{\sin^2 \theta_i - 2\sqrt{1 - \frac{T}{E_0}} \sin\theta_i \cos\phi \sin\alpha + \left(1 - \frac{T}{E_0}\right) \sin^2 \alpha} \quad (\text{A.12})$$

Hence, the surface scattering probability is:

$$\frac{d^2 P}{d\Omega \cdot dT} = \frac{k_0^2}{\pi^2 a_0 m_0 v^2} \frac{k_0 \sqrt{\sin^2 \theta_i - 2\sqrt{1 - \frac{T}{E_0}} \sin\theta_i \cos\phi \sin\alpha + \left(1 - \frac{T}{E_0}\right) \sin^2 \alpha}}{4k_0^4 \left(1 - \frac{T}{2E_0} - 2\sqrt{1 - \frac{T}{E_0}} \cos\theta\right)^2 \cos\theta_i} \text{Im}\left(\frac{1}{\varepsilon(T)} - \frac{4}{1 + \varepsilon(T)}\right) \quad (\text{A.13})$$

After integration over all photoelectron incidence angles, the differential scattering probability for surface plasmon excitation is given by:

$$\frac{dP}{dT} = \frac{g(T, \alpha)}{2\pi^2 a_0 k_0 E_0} \text{Im} \left( \frac{1}{\varepsilon(T)} - \frac{4}{1 + \varepsilon(T)} \right) \quad (\text{A.14})$$

$$(\text{A.15})$$

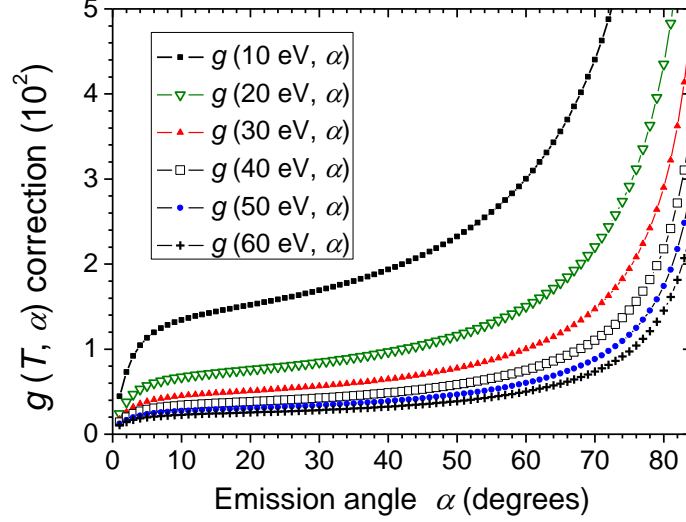


**Fig. A.3:** Angular correction  $g(T, \alpha)$  for inelastic scattering at different surface loss energies.

The sensitivity factor  $g(T, \alpha)$  for XPS is determined using the number of photo-electrons scattered at the interface over solid angle  $d\Omega = \sin\theta_i d\theta_i d\varphi$  and entering the analyzer at polar angle  $\alpha$ . For small  $\theta$  values, as obtained in plasmon excitation, approximations  $\gamma \approx \gamma_0$ ,  $\phi \approx 0$  and  $\alpha \approx \theta_i$  greatly simplify integrations over  $\theta_i$  and  $\varphi$  angles:

$$g(T, \alpha) = \int_{\alpha - \delta\alpha}^{\alpha + \delta\alpha} \int_{-\delta\varphi}^{\delta\varphi} \frac{\sqrt{\sin^2\theta_i - 2\sqrt{1 - \frac{T}{E_0}} \sin\theta_i \cos\varphi \sin\alpha + \left(1 - \frac{T}{E_0}\right) \sin^2\alpha}}{4 \left(1 - \frac{T}{2E_0} - 2\sqrt{1 - \frac{T}{E_0}} \cos\theta\right)^2 \cos\theta_i} \sin(\theta_i) d\varphi d\theta_i \quad (\text{A.15})$$

The solution  $g(T, \alpha)$  was calculated numerically ; an analytical approximation given by

$$g(T, \alpha) = \frac{E_0}{T \cos\alpha} \left[ \frac{2T}{E_0} \pi + \left(1 - \frac{4T}{E_0}\right) \arctan \left( 8\pi \alpha \sqrt{1 - \frac{4T}{E_0}} \right) \right] \quad (\text{A.16})$$

empirically matches exact results within 1%. The Bethe-Born factor shown in **Figure A.3** for several surface loss energies reveal that: (i)  $g(T, \alpha)$  follows a  $1/T$  law for  $\alpha \geq 10^\circ$  where the second

term value in the bracket dominates, (ii) it behaves as  $1/\cos\alpha$  in the  $\alpha \geq 10^\circ$  region and converges towards  $2\pi$  for  $\alpha \ll 10^\circ$ .

This correction function  $g(T, \alpha)$  is used in **step 7** of the algorithm in order to estimate the surface plasmon contribution to the total energy loss spectrum and refine the determination of the dielectric function. In principle, its use is only valid in the case of a perfectly planar surface.

## Appendix B: Cutoff angle and cutoff wave vector

Above a critical wave vector  $q_C$ , plasma oscillations are strongly damped due to some energy transfer to single-electron excitations (electron-hole pairs) [2]. This cutoff wave number can be

determined in a Free Electron (FE) model with Fermi energy  $E_F = \frac{\hbar^2}{2m_0} k_F^2 = \frac{\hbar^2}{2m_0} (3\pi^2 n_e)^{2/3}$ . The

plasmon energy  $E_p(q)$  at which  $\varepsilon_1$  crosses zero is given by the dispersion relation

$E_p(q) = E_p + \eta \frac{\hbar^2}{m_0} q^2$  with a dispersion coefficient  $\eta = \frac{3 E_F}{5 E_p}$ . Energy conservation rules provide

a critical wave vector (if  $\eta \approx 0.5$ ):

$$q_C \approx \frac{m_0 E_p}{\hbar^2 k_F} = \frac{E_p}{\hbar v_F} \quad (\text{B.1})$$

where  $v_F$  is the Fermi velocity.

For a dense amorphous carbon, with valence electron density  $n_e = 6.4 \times 10^{29} m^{-3}$ , one obtains

$E_p = 29.7 eV$ ,  $E_F = 27.1 eV$ ,  $v_F = 3.1 \cdot 10^6 m/s$  and  $\eta = 0.508$ . Hence  $q_C = 14.6 nm^{-1}$  provides a

critical angle  $\theta_c \approx \frac{q_C}{k_0}$  of 90 mrd (for C1s photoelectrons excited by Mg K $\alpha$  X-rays).

For silicon with valence electron density  $n_e = 2.0 \times 10^{29} m^{-3}$ ,  $E_p = 17.2 eV$ ,  $E_F = 13.1 eV$ ,

$v_F = 2.14 \cdot 10^6 m/s$  and  $\eta = 0.405$ . Hence  $q_C = 12.2 nm^{-1}$  provides a critical angle  $\theta_c \approx \frac{q_C}{k_0}$  of 75

mrd (for Si2p photoelectrons excited by Mg K $\alpha$  X-rays).

Some changes in  $q_C$  values are expected either from dispersion effects (deviation of the approximation  $\eta \approx 0.5$ ) or from band structure effects.

## Appendix C: Determination of the dielectric function and inelastic mean free paths

The dielectric function formalism for electron scattering by surface and bulk plasmon excitation is briefly recalled for XPS-PEELS. Sum rules are applied to the dielectric function and inelastic the mean free path (or scattering cross section) is further determined.

### (1) Kramers-Krönig analysis of the dielectric function

After deconvolution of multiple plasmon scattering, the measured energy-loss distribution due to a single bulk plasmon excitation,  $S_B(T)$  is proportional to  $K(E_0, T)$  given by **Eq. (A.7)** and to the core level photoelectron flux,  $I_0$ :

$$S_B(T) = \lambda_p I_0 K_p(E_0, T) = \lambda_p I_0 \frac{f_c(T)}{2\pi^2 a_0 E_0} \text{Im}\left(-\frac{1}{\varepsilon(T)}\right) \quad (\text{C.1})$$

where  $\lambda_p$  is the total inelastic scattering free path,  $E_0$  is the kinetic energy of the primary photoelectrons,  $n_A$  and  $\varepsilon(T)$  are respectively the atom density and the dielectric function of the material,  $a_0$  is the Bohr radius and  $f_c(T)$  is the Born-Bethe factor calculated in **Appendix B**. The dielectric function obeys the Kramers-Krönig relation:

$$\text{Re}\left(\frac{1}{\varepsilon(T)}\right) = 1 - \frac{2}{\pi} \int_0^\infty \text{Im}\left(-\frac{1}{\varepsilon(T')}\right) \frac{T' dT'}{T'^2 - T^2} \quad (\text{C.2})$$

Using this relation with  $T = 0$ ,

$$1 - \text{Re}\left(\frac{1}{\varepsilon(0)}\right) = 1 - \frac{1}{n^2} = \frac{2}{\pi} \int_0^\infty \text{Im}\left(-\frac{1}{\varepsilon(T)}\right) \frac{dT}{T} \quad (\text{C.3})$$

**Eq. (C.3)** allows determination of absolute values of  $\text{Im}\left(-\frac{1}{\varepsilon(T)}\right)$  if the refractive index  $n(0)$  of the material in the sub-gap energy range can be measured independently, e.g. by optical methods. Substituting the integral by a discrete sum and using **Eq. (C.1)**, one obtains:

$$\frac{\pi}{2} \left(1 - \frac{1}{n^2}\right) = \frac{2\pi^2 a_0 E_0}{\lambda_p I_0} \sum \frac{S_B(T)}{f_c(T)} \frac{\delta T}{T} \quad (\text{C.4})$$

where  $E_0$ ,  $T$  and  $S_B(T)$  are measured by XPS and  $\delta T$  is the elementary energy step. Using this relationship in **Eq. (C.1)**, we find:

$$\text{Im}\left(-\frac{1}{\varepsilon(T)}\right) = \frac{\frac{\pi}{2}\left(1 - \frac{1}{n^2}\right) \frac{S_B(T)}{f(T)}}{\sum_0^N \frac{S_B(T)}{f_c(T) T} \delta T}. \quad (\text{C.5})$$

Note that uncertainties on  $S_B(T)$  at low  $T$  values may strongly affect the denominator, hence the first terms in the sum must usually be suppressed. Once  $\text{Im}\left(\frac{-1}{\varepsilon(T)}\right)$  has been computed, its real part is derived by applying the Kramers-Krönig relationship **Eq. (C.2)**. If necessary, a suitable power-law extrapolation is performed beyond the measurement energy range. Then one obtains the complex permittivity ( $\varepsilon_1(T)$ ,  $\varepsilon_2(T)$ ) or the complex refractive index ( $n(T)$ ,  $k(T)$ ).

## (2) Surface plasmon contribution

At a planar solid-vacuum boundary, the differential scattering probability for surface plasmon excitation is given by **Eq. (A.14)** and the surface Bethe-Born factor  $g(T, \alpha)$  (**Eq. (A.15)**). The intensity of the signal due to the surface plasmon is:

$$S_s(T) = I_0 \frac{dP}{dT} = \frac{g(T, \alpha) I_0}{2\pi^2 a_0 k_0 E_0} \text{Im}\left(\frac{1}{\varepsilon(T)} - \frac{4}{1 + \varepsilon(T)}\right) \quad (\text{C.6})$$

where  $k_0$  is the wave vector of the primary photoelectrons and  $\alpha$  is the angle between the sample surface normal and the detector axis.

Once an estimate of the dielectric function is obtained,  $S_s(T)$  is computed and subtracted from the total loss signal in order to determine a new corrected value of the volume signal which is injected as a new input in the deconvolution process (**step 3** of the algorithm). The surface loss amplitude and a self-consistent  $\varepsilon(T)$  are obtained after a few iterations.

**Figure C.1** shows the loss function and its Kramers-Krönig transform. It also illustrates the fact that spectral distributions  $S_s(T)$  and  $S_B(T)$  overlap in the same loss energy range. The surface scattering probability exhibits a negative term proportional to  $\text{Im}\left(\frac{1}{\varepsilon(T)}\right)$  which means that surface scattering reduces the volume scattering probability near  $E_P$ . On the other hand, the positive term  $\text{Im}\left(-\frac{4}{1 + \varepsilon(T)}\right)$ , with a maximum located below the plasmon peak, increases the loss signal at lower energies.

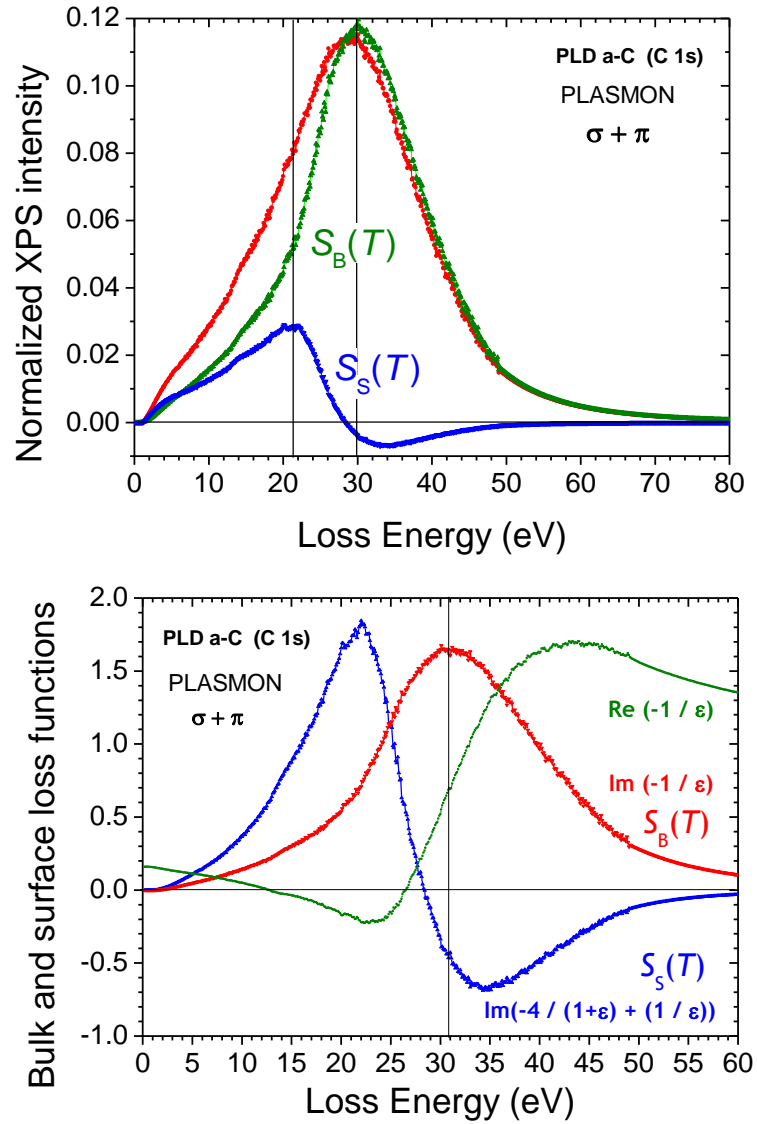


**Fig. C.1:** Self-consistent separation of bulk and surface losses (a) using a Kramers-Krönig analysis (b) of XPS-PEELS data after deconvolution of multiple plasmon losses in PLD a-C ( $\alpha = 0^\circ$ ).

### (3) Sum rules

The effective number of electrons,  $N_{\text{EFF}}$ , involved in the dielectric function is determined applying the Bethe sum rules [72]:

$$N_1 = \frac{2\varepsilon_0 m_0}{\pi \hbar^2 N_{AT}} \int_0^\infty \text{Re}(\varepsilon(T)) T dT \quad (\text{C.7})$$

$$N_2 = \frac{2\varepsilon_0 m_0}{\pi \hbar^2 N_{AT}} \int_0^\infty \text{Im} \left( -\frac{1}{\varepsilon(T)} \right) T \, dT \quad (\text{C.8})$$

The latter equation is known as the oscillator strength or  $f$ -sum rule.

#### (4) Determination of inelastic mean free paths

From the ELF we can derive the IMFP for volume plasmon excitation,  $\lambda_p(E_0)$ , defined by **Eq. 3**,

or the cross section  $\sigma_p = \frac{1}{\lambda_p N_{AT}}$  if the atom density  $N_{AT}$  is known:

$$\frac{1}{\lambda_p} = \int_0^\infty \frac{f_C(T)}{2\pi^2 a_0 E_0} \text{Im} \left( -\frac{1}{\varepsilon(T)} \right) dT \quad (\text{C.9})$$

Using **Eq (C.5)**, we can calculate the inverse IMFP :

$$\frac{1}{\lambda_p} = \frac{\left(1 - \frac{1}{n^2}\right)}{4\pi a_0 E_0} \frac{\sum S_B(T) \delta T}{\sum_T \frac{S_B(T)}{f_C(T)} \delta T} \quad (\text{C.10})$$

## REFERENCES

- [1] R.H. Ritchie, *Phys. Rev.* 106 (1957) 874.
- [2] H. Raether, *Excitation of Plasmons and Interband Transitions by Electrons*, Springer Tracts in Modern Physics vol. 88, Springer-Verlag, Berlin, 1997.
- [3] R.F. Egerton, *Electron Energy-Loss Spectroscopy in the Electron Microscope*, Plenum Press, New York, 1986.
- [4] J. Daniels, C.v. Festenberg, H. Raether, K. Zeppenfeld, Springer Tracts in Modern Physics vol. 54, Springer-Verlag, Berlin, 1970, p. 77.
- [5] S. Hufner: *Photoelectron Spectroscopy*, Springer series in Solid-State Sciences vol. 82, Springer, Berlin, 1995.
- [6] D.E. Aspnes, *Spectroscopic Ellipsometry of Solids*. In: *Optical Properties of Solids: New Developments* (B.O. Seraphin, ed.). North-Holland, Amsterdam, 1976.
- [7] J.N. Israelachvili, *Intermolecular and Surface Forces*, 2nd edition, Academic Press, London, 1992.
- [8] C.J. van Oss, *Interfacial forces in aqueous media*, Marcel Dekker, New York, 1994.
- [9] W.S.M. Werner, A. Ruocco, F. Offi, S. Iacobucci, W. Smekal, H. Winter, G. Stefani, *Phys. Rev. B* 78 (2008) 233403.
- [10] W.S.M. Werner, *Surf. Interf. Anal.* 31 (2001) 141–176.
- [11] R.F. Egerton, *Rep. Prog. Phys.* 72 (2009) 016502.
- [12] D.R. Penn, *Phys. Rev. Lett.* 38 (1977) 1429–1432.
- [13] P. Steiner, H. Höchst, S. Hüfner, *Z. Phys. B* 30 (1978) 129.
- [14] J. Fink, Th. Müller-Heinzerling, J. Pflüger, B. Scheerer, B. Dischler, P. Koidl, A. Bubenzer, R.E. Sah, *Phys. Rev. B* 30 (1984) 4713.
- [15] S. Waidmann, M. Knupfer, J. Fink, B. Kleinsorge, J. Robertson, *Diamond Relat. Mater.* 9 (2000) 722.
- [16] V. Stolojan, *Amorphous Carbon and its properties*. In: S.R.P. Silva, Editor, *EMIS Datareviews Series 29*, INSPEC, 2002, p. 83.
- [17] C. Godet, D. David, H. Sabbah, S. Ababou-Girard, F. Solal, *Appl. Surf. Sci.* 255 (2009) 6598.
- [18] A. Cohen Simonsen, F. Yubero, S. Tougaard, *Phys. Rev. B* 56 (1997) 1612–1619.
- [19] W.S.M. Werner, P. Schattschneider, *J. Electron Spectrosc. Relat. Phen.* 143 (2005) 65–80.
- [20] S. Tougaard, I. Chorkendorff, *Phys. Rev. B.* 35 (1987) 6570.
- [21] S. Tougaard, *Surf. Interf. Anal.* 11 (1988) 453–472.
- [22] S. Tougaard, *J. Electron Spectrosc. Relat. Phen.* 178-179 (2010) 128–153.
- [23] T. Fujikawa, M. Kazama, H. Shinotsuka, *e-J. Surf. Sci. Nanotech.* 6 (2008) 263.
- [24] C.N Berglund, W.E. Spicer, *Phys. Rev. A* 136 (1964) 1030.
- [25] S. Doniach, M. Sunjic, *J. Phys. C* 3 (1970) 285.

- [26] D. David, C. Godet, H. Sabbah, S. Ababou-Girard, F. Solal, V. Chu, J.P. Conde, *J. Non-Cryst. Solids* 358 (2012) 2019.
- [27] J. Robertson, *Mat. Sci. Eng. R* 37 (2002) 129–281.
- [28] A. Zebda, H. Sabbah, S. Ababou-Girard, F. Solal, C. Godet, *Appl. Surf. Sci.* 254 (2008) 4980.
- [29] H. Jin, H. Yoshikawa, S. Tanuma, S. Tougaard, *Surf. Interf. Anal.* 42 (2010) 1076.
- [30] W.S.M. Werner, W. Smekal, H. Störi, C. E. Eisenmenger-Sittner, *J. Vac. Sci. Technol. A* 19 (2001) 2388.
- [31] W.S.M. Werner, W. Smekal, C. Tomastik, H. Stori, *Surf. Sci.* 486 (2001) L461-466.
- [32] N. Pauly, S. Tougaard, *Surf. Interf. Anal.* 41 (2009) 735.
- [33] N. Pauly, S. Tougaard, *Surf. Sci.* 603 (2009) 2158-2162.
- [34] C. Klauber, *Appl. Surf. Sci.* 70/71 (1993) 35–39.
- [35] G.D. Mahan, *Phys. Rev. B* 11 (1975) 4814.
- [36] P. Nozières, C.T. de Dominicis, *Phys. Rev.* 178 (1969) 1097.
- [37] T.T.P. Cheung, *J. Appl. Phys.* 53 (1982) 6857.
- [38] V. Chu, J.P. Conde, J. Jarego, P. Brogueira, J. Rodriguez, N. Barradas, J.C. Soares, *J. Appl. Phys.* 78 (1995) 3164.
- [39] H. Sabbah, S. Ababou-Girard, A. Zebda, D. David, B. Fabre, S. Députier, A. Perrin, M. Guilloux-Viry, F. Solal, C. Godet, *Diam. Relat. Mater.* 18 (2009) 1074.
- [40] M. Clin, O. Durand-Drouhin, A. Zeinert, J.C. Picot, *Diam. Relat. Mater.* 8 (1999) 527.
- [41] T. Katsuno, C. Godet, J.C. Orlianges, A.-S. Loir, F. Garrelie, A. Catherinot, *Appl. Phys. A* 81 (2005) 471–476.
- [42] S. Tougaard, *Surf. Interf. Anal.* 25 (1997) 137–154.
- [43] S. Waidmann, M. Knupfer, J. Fink, B. Kleinsorge, J. Robertson, *J. Appl. Phys.* 89 (2001) 3783.
- [44] A.G. Marinopoulos, L. Reining, V. Olevano, A. Rubio, T. Pichler, X. Liu, M. Knupfer, J. Fink, *Phys. Rev. Lett.* 89 (2002) 076402.
- [45] E.T. Arakawa, S.M. Dolfini, J.C. Ashley, M.W. Williams, *Phys. Rev. B* 31 (1985) 8097.
- [46] C. Gao, Y.Y. Wang, A.L. Ritter, J.R. Dennison, *Phys. Rev. Lett.* 62 (1989) 945.
- [47] M.L. Thèye, V. Paret, A. Sadki, *Diamond Relat. Mater.* 10 (2001) 182.
- [48] G. Fanchini, A. Tagliaferro, N. Conway, C. Godet, *Phys. Rev. B* 66 (2002) 195415.
- [49] S. Kassavetis, P. Patsalas, S. Logothetidis, J. Robertson, S. Kennou, *Diamond Relat. Mater.* 16 (2007) 1813-1822.
- [50] C.J. Powell, A. Jablonski, *J. Phys. Chem. Ref. Data* 19 (1999) 28.
- [51] C.J. Powell, *J. Electron Spectrosc. Rel. Phen.* 47 (1988) 197.
- [52] W.S.M. Werner, C. Tomastik, T. Cabela, G. Richter, H. Stori, *J. Electron Spectrosc. Relat. Phen.* 113 (2001) 127.

- [53] S. Tanuma, C.J. Powell, D.R. Penn, *J. Electron Spectrosc. Relat. Phenom.* 62 (1993) 95.
- [54] S. Tanuma, C.J. Powell, D.R. Penn, *Surf. Interf. Anal.* 17 (1991) 929.
- [55] S. Tanuma, C.J. Powell, D.R. Penn, *Surf. Interf. Anal.* 36 (2004) 1–14.
- [56] D.R. Penn, *Phys. Rev. B* 35 (1987) 482.
- [57] H. Bethe, *Ann. Phys.* 5 (1930) 325.
- [58] S. Tanuma, C.J. Powell, D.R. Penn, *Surf. Interf. Anal.* 21 (1994) 165.
- [59] S. Tanuma, C. J. Powell, D. R. Penn, *Surf. Interf. Anal.* 11 (1988) 577–589.
- [60] J. Zemek, J. Potmesil, M. Vanecek, B. Lesiak, A. Jablonski, *Appl. Phys. Lett.* 87 (2005) 262114.
- [61] S. Tanuma, T. Shiratori, T. Kimura, K. Goto, S. Ichimura, C.J. Powell, *Surf. Interf. Anal.* 37 (2005) 833-845.
- [62] A. Jablonski, C.J. Powell, *Surf. Sci.* 606 (2012) 644–651.
- [63] L. Calliari, S. Fanchenko, *Surf. Interf. Anal.* 44 (2012) 1104–1109.
- [64] A.C. Ferrari, A. Libassi, B.K. Tanner, V. Stolojan, J. Yuan, L.M. Brown, S.E. Rodil, B. Kleinsorge, J. Robertson, *Phys. Rev. B* 62 (2000) 11089.
- [65] N. Marks, *J. Phys.: Condens. Matter* 14 (2002) 2901–2927.
- [66] Z. Remes, M. Vanecek, A.H. Mahan, R.S. Crandall, *Phys. Rev. B.* 56 (1997) R12710.
- [67] N. Pauly, S. Tougaard, *Surf. Sci.* 602 (2008) 1974.
- [68] D.G.F. David, J.S.R.Guerreiro, M.V.S. Silva, P. Bargiela, J.S. Almeida, J.A. Freitas, A.F. Silva, *J. Cryst. Growth* 350 (2012) 11–16.
- [69] M.V.S. Silva, D.G.F. David, I.M. Pepe, A.F. Silva, J.S. Almeida, A.L. Gazoto, L.P. Cardoso, E.A. Menezes, D.L. Graybill, K.M. Mertes, *Thin Solid Films* 520 (2012) 4848–4852.
- [70] J.H. Scofield, *J. Electron Spectrosc. Relat. Phen.* 8 (1976) 129.
- [71] J.W. Cooper, *Phys. Rev. B* 47 (1993) 1841.
- [72] D.Y. Smith, E. Shiles, *Phys. Rev. B* 17 (1978) 4689.